

## Diffractive jet production in deep-inelastic $e^+p$ collisions at HERA

The H1 Collaboration

C. Adloff<sup>33</sup>, V. Andreev<sup>24</sup>, B. Andrieu<sup>27</sup>, T. Anthonis<sup>4</sup>, V. Arkadov<sup>35</sup>, A. Astvatsatourov<sup>35</sup>, I. Ayyaz<sup>28</sup>, A. Babaev<sup>23</sup>, J. Bähr<sup>35</sup>, P. Baranov<sup>24</sup>, E. Barrelet<sup>28</sup>, W. Bartel<sup>10</sup>, P. Bate<sup>21</sup>, A. Beglarian<sup>34</sup>, O. Behnke<sup>13</sup>, C. Beier<sup>14</sup>, A. Belousov<sup>24</sup>, T. Benisch<sup>10</sup>, Ch. Berger<sup>1</sup>, T. Berndt<sup>14</sup>, J.C. Bizot<sup>26</sup>, V. Boudry<sup>27</sup>, W. Braunschweig<sup>1</sup>, V. Brisson<sup>26</sup>, H.-B. Bröker<sup>2</sup>, D.P. Brown<sup>11</sup>, W. Brückner<sup>12</sup>, P. Bruel<sup>27</sup>, D. Bruncko<sup>16</sup>, J. Bürger<sup>10</sup>, F.W. Büsler<sup>11</sup>, A. Bunyatyan<sup>12,34</sup>, H. Burkhardt<sup>14</sup>, A. Burrage<sup>18</sup>, G. Buschhorn<sup>25</sup>, A.J. Campbell<sup>10</sup>, J. Cao<sup>26</sup>, T. Carli<sup>25</sup>, S. Caron<sup>1</sup>, E. Chabert<sup>22</sup>, D. Clarke<sup>5</sup>, B. Clerbaux<sup>4</sup>, C. Collard<sup>4</sup>, J.G. Contreras<sup>7,41</sup>, Y.R. Coppens<sup>3</sup>, J.A. Coughlan<sup>5</sup>, M.-C. Cousinou<sup>22</sup>, B.E. Cox<sup>21</sup>, G. Cozzika<sup>9</sup>, J. Cvach<sup>29</sup>, J.B. Dainton<sup>18</sup>, W.D. Dau<sup>15</sup>, K. Daum<sup>33,39</sup>, M. Davidsson<sup>20</sup>, B. Delcourt<sup>26</sup>, N. Delerue<sup>22</sup>, R. Demirchyan<sup>34</sup>, A. De Roeck<sup>10,43</sup>, E.A. De Wolf<sup>4</sup>, C. Diaconu<sup>22</sup>, P. Dixon<sup>19</sup>, V. Dodonov<sup>12</sup>, J.D. Dowell<sup>3</sup>, A. Drutskoi<sup>23</sup>, C. Duprel<sup>2</sup>, G. Eckerlin<sup>10</sup>, D. Eckstein<sup>35</sup>, V. Efremenko<sup>23</sup>, S. Egli<sup>32</sup>, R. Eichler<sup>36</sup>, F. Eisele<sup>13</sup>, E. Eisenhandler<sup>19</sup>, M. Ellerbrock<sup>13</sup>, E. Elsen<sup>10</sup>, M. Erdmann<sup>10,40,e</sup>, W. Erdmann<sup>36</sup>, P.J.W. Faulkner<sup>3</sup>, L. Favart<sup>4</sup>, A. Fedotov<sup>23</sup>, R. Felst<sup>10</sup>, J. Ferencei<sup>10</sup>, S. Ferron<sup>27</sup>, M. Fleischer<sup>10</sup>, Y.H. Fleming<sup>3</sup>, G. Flügge<sup>2</sup>, A. Fomenko<sup>24</sup>, I. Foresti<sup>37</sup>, J. Formánek<sup>30</sup>, J.M. Foster<sup>21</sup>, G. Franke<sup>10</sup>, E. Gabathuler<sup>18</sup>, K. Gabathuler<sup>32</sup>, J. Garvey<sup>3</sup>, J. Gassner<sup>32</sup>, J. Gayler<sup>10</sup>, R. Gerhards<sup>10</sup>, S. Ghazaryan<sup>34</sup>, L. Goerlich<sup>6</sup>, N. Gogitidze<sup>24</sup>, M. Goldberg<sup>28</sup>, C. Goodwin<sup>3</sup>, C. Grab<sup>36</sup>, H. Grässler<sup>2</sup>, T. Greenshaw<sup>18</sup>, G. Grindhammer<sup>25</sup>, T. Hadig<sup>13</sup>, D. Haidt<sup>10</sup>, L. Hajduk<sup>6</sup>, W.J. Haynes<sup>5</sup>, B. Heinemann<sup>18</sup>, G. Heinzelmann<sup>11</sup>, R.C.W. Henderson<sup>17</sup>, S. Hengstmann<sup>37</sup>, H. Henschel<sup>35</sup>, R. Heremans<sup>4</sup>, G. Herrera<sup>7,41</sup>, I. Herynek<sup>29</sup>, M. Hildebrandt<sup>37</sup>, M. Hilgers<sup>36</sup>, K.H. Hiller<sup>35</sup>, J. Hladký<sup>29</sup>, P. Höting<sup>2</sup>, D. Hoffmann<sup>10</sup>, R. Horisberger<sup>32</sup>, S. Hurling<sup>10</sup>, M. Ibbotson<sup>21</sup>, Ç. İşsever<sup>7</sup>, M. Jacquet<sup>26</sup>, M. Jaffre<sup>26</sup>, L. Janauschek<sup>25</sup>, D.M. Jansen<sup>12</sup>, X. Janssen<sup>4</sup>, V. Jemanov<sup>11</sup>, L. Jönsson<sup>20</sup>, D.P. Johnson<sup>4</sup>, M.A.S. Jones<sup>18</sup>, H. Jung<sup>10</sup>, H.K. Kästli<sup>36</sup>, D. Kant<sup>19</sup>, M. Kapichine<sup>8</sup>, M. Karlsson<sup>20</sup>, O. Karschnick<sup>11</sup>, F. Keil<sup>14</sup>, N. Keller<sup>37</sup>, J. Kennedy<sup>18</sup>, I.R. Kenyon<sup>3</sup>, S. Kermiche<sup>22</sup>, C. Kiesling<sup>25</sup>, P. Kjellberg<sup>20</sup>, M. Klein<sup>35</sup>, C. Kleinwort<sup>10</sup>, G. Knies<sup>10</sup>, B. Koblitz<sup>25</sup>, S.D. Kolya<sup>21</sup>, V. Korbel<sup>10</sup>, P. Kostka<sup>35</sup>, S.K. Kotelnikov<sup>24</sup>, R. Koutouev<sup>12</sup>, A. Koutov<sup>8</sup>, M.W. Krasny<sup>28</sup>, H. Krehbiel<sup>10</sup>, J. Kroseberg<sup>37</sup>, K. Krüger<sup>10</sup>, A. Küpper<sup>33</sup>, T. Kuhr<sup>11</sup>, T. Kurča<sup>35,16</sup>, R. Lahmann<sup>10</sup>, D. Lamb<sup>3</sup>, M.P.J. Landon<sup>19</sup>, W. Lange<sup>35</sup>, T. Laštovička<sup>30</sup>, P. Laycock<sup>18</sup>, E. Lebailly<sup>26</sup>, A. Lebedev<sup>24</sup>, B. Leißner<sup>1</sup>, R. Lemrani<sup>10</sup>, V. Lendermann<sup>7</sup>, S. Levonian<sup>10</sup>, M. Lindstroem<sup>20</sup>, B. List<sup>36</sup>, E. Lobodzinska<sup>10,6</sup>, B. Lobodzinski<sup>6,10</sup>, A. Loginov<sup>23</sup>, N. Loktionova<sup>24</sup>, V. Lubimov<sup>23</sup>, S. Lüders<sup>36</sup>, D. Lüke<sup>7,10</sup>, L. Lytkin<sup>12</sup>, N. Magnussen<sup>33</sup>, H. Mahlke-Krüger<sup>10</sup>, N. Malden<sup>21</sup>, E. Malinovski<sup>24</sup>, I. Malinovski<sup>24</sup>, R. Maraček<sup>25</sup>, P. Marage<sup>4</sup>, J. Marks<sup>13</sup>, R. Marshall<sup>21</sup>, H.-U. Martyn<sup>1</sup>, J. Martyniak<sup>6</sup>, S.J. Maxfield<sup>18</sup>, A. Mehta<sup>18</sup>, K. Meier<sup>14</sup>, P. Merkel<sup>10</sup>, A.B. Meyer<sup>11</sup>, H. Meyer<sup>33</sup>, J. Meyer<sup>10</sup>, P.-O. Meyer<sup>2</sup>, S. Mikocki<sup>6</sup>, D. Milstead<sup>18</sup>, T. Mkrtchyan<sup>34</sup>, R. Mohr<sup>25</sup>, S. Mohr dieck<sup>11</sup>, M.N. Mondragon<sup>7</sup>, F. Moreau<sup>27</sup>, A. Morozov<sup>8</sup>, J.V. Morris<sup>5</sup>, K. Müller<sup>13</sup>, P. Murin<sup>16,42</sup>, V. Nagovizin<sup>23</sup>, B. Naroska<sup>11</sup>, J. Naumann<sup>7</sup>, Th. Naumann<sup>35</sup>, G. Nellen<sup>25</sup>, P.R. Newman<sup>3</sup>, T.C. Nicholls<sup>5</sup>, F. Niebergall<sup>11</sup>, C. Niebuhr<sup>10</sup>, O. Nix<sup>14</sup>, G. Nowak<sup>6</sup>, T. Nunnemann<sup>12</sup>, J.E. Olsson<sup>10</sup>, D. Ozerov<sup>23</sup>, V. Panassik<sup>8</sup>, C. Pascaud<sup>26</sup>, G.D. Patel<sup>18</sup>, E. Perez<sup>9</sup>, J.P. Phillips<sup>18</sup>, D. Pitzl<sup>10</sup>, R. Pöschl<sup>7</sup>, I. Potachnikova<sup>12</sup>, B. Povh<sup>12</sup>, K. Rabbertz<sup>1</sup>, G. Rädcl<sup>1</sup>, J. Rauschenberger<sup>11</sup>, P. Reimer<sup>29</sup>, B. Reiser<sup>25</sup>, D. Reyna<sup>10</sup>, S. Riess<sup>11</sup>, C. Risler<sup>25</sup>, E. Rizvi<sup>3</sup>, P. Robmann<sup>37</sup>, R. Roosen<sup>4</sup>, A. Rostovtsev<sup>23</sup>, C. Royon<sup>9</sup>, S. Rusakov<sup>24</sup>, K. Rybicki<sup>6</sup>, D.P.C. Sankey<sup>5</sup>, J. Scheins<sup>1</sup>, F.-P. Schilling<sup>13</sup>, P. Schleper<sup>10</sup>, D. Schmidt<sup>33</sup>, D. Schmidt<sup>10</sup>, S. Schmitt<sup>10</sup>, L. Schoeffel<sup>9</sup>, A. Schönig<sup>36</sup>, T. Schörner<sup>25</sup>, V. Schröder<sup>10</sup>, H.-C. Schultz-Coulon<sup>7</sup>, C. Schwabenberger<sup>10</sup>, K. Sedláč<sup>29</sup>, F. Sefkow<sup>37</sup>, V. Shekelyan<sup>25</sup>, I. Sheviakov<sup>24</sup>, L.N. Shtarkov<sup>24</sup>, P. Sievers<sup>13</sup>, Y. Sirois<sup>27</sup>, T. Sloan<sup>17</sup>, P. Smirnov<sup>24</sup>, V. Solochenko<sup>23,†</sup>, Y. Soloviev<sup>24</sup>, V. Spaskov<sup>8</sup>, A. Specka<sup>27</sup>, H. Spitzer<sup>11</sup>, R. Stamen<sup>7</sup>, J. Steinhart<sup>11</sup>, B. Stella<sup>31</sup>, A. Stellberger<sup>14</sup>, J. Stiewe<sup>14</sup>, U. Straumann<sup>37</sup>, W. Struczinski<sup>2</sup>, M. Swart<sup>14</sup>, M. Taševský<sup>29</sup>, V. Tchernyshov<sup>23</sup>, S. Tchetchelnitski<sup>23</sup>, G. Thompson<sup>19</sup>, P.D. Thompson<sup>3</sup>, N. Tobien<sup>10</sup>, D. Traynor<sup>19</sup>, P. Truöl<sup>37</sup>, G. Tsipolitis<sup>10,38</sup>, I. Tsurin<sup>35</sup>, J. Turnau<sup>6</sup>, J.E. Turney<sup>19</sup>, E. Tzamariudaki<sup>25</sup>, S. Udluft<sup>25</sup>, A. Usik<sup>24</sup>, S. Valkár<sup>30</sup>, A. Valkárová<sup>30</sup>, C. Vallée<sup>22</sup>, P. Van Mechelen<sup>4</sup>, S. Vassiliev<sup>8</sup>, Y. Vazdik<sup>24</sup>, A. Vichnevski<sup>8</sup>, K. Wacker<sup>7</sup>, R. Wallny<sup>37</sup>, T. Walter<sup>37</sup>, B. Waugh<sup>21</sup>, G. Weber<sup>11</sup>, M. Weber<sup>14</sup>, D. Wegener<sup>7</sup>, M. Werner<sup>13</sup>, G. White<sup>17</sup>, S. Wiesand<sup>33</sup>, T. Wilksen<sup>10</sup>, M. Winde<sup>35</sup>, G.-G. Winter<sup>10</sup>, Ch. Wissing<sup>7</sup>, M. Wobisch<sup>2</sup>, H. Wollatz<sup>10</sup>, E. Wünsch<sup>10</sup>, A.C. Wyatt<sup>21</sup>, J. Žáček<sup>30</sup>, J. Zálesák<sup>30</sup>, Z. Zhang<sup>26</sup>, A. Zhokin<sup>23</sup>, F. Zomer<sup>26</sup>, J. Zembery<sup>9</sup>, M. zur Nedden<sup>10</sup>

<sup>1</sup> I. Physikalisches Institut der RWTH, Aachen, Germany<sup>a</sup>

<sup>2</sup> III. Physikalisches Institut der RWTH, Aachen, Germany<sup>a</sup>

<sup>3</sup> School of Physics and Space Research, University of Birmingham, Birmingham, UK<sup>b</sup>

- <sup>4</sup> Inter-University Institute for High Energies ULB-VUB, Brussels; Universitaire Instelling Antwerpen, Wilrijk; Belgium<sup>c</sup>  
<sup>5</sup> Rutherford Appleton Laboratory, Chilton, Didcot, UK<sup>b</sup>  
<sup>6</sup> Institute for Nuclear Physics, Cracow, Poland<sup>d</sup>  
<sup>7</sup> Institut für Physik, Universität Dortmund, Dortmund, Germany<sup>a</sup>  
<sup>8</sup> Joint Institute for Nuclear Research, Dubna, Russia  
<sup>9</sup> CEA, DSM/DAPNIA, CE-Saclay, Gif-sur-Yvette, France  
<sup>10</sup> DESY, Hamburg, Germany<sup>a</sup>  
<sup>11</sup> II. Institut für Experimentalphysik, Universität Hamburg, Hamburg, Germany<sup>a</sup>  
<sup>12</sup> Max-Planck-Institut für Kernphysik, Heidelberg, Germany<sup>a</sup>  
<sup>13</sup> Physikalisches Institut, Universität Heidelberg, Heidelberg, Germany<sup>a</sup>  
<sup>14</sup> Kirchhoff-Institut für Physik, Universität Heidelberg, Heidelberg, Germany<sup>a</sup>  
<sup>15</sup> Institut für experimentelle und angewandte Kernphysik, Universität Kiel, Kiel, Germany<sup>a</sup>  
<sup>16</sup> Institute of Experimental Physics, Slovak Academy of Sciences, Košice, Slovak Republic<sup>e,f</sup>  
<sup>17</sup> School of Physics and Chemistry, University of Lancaster, Lancaster, UK<sup>b</sup>  
<sup>18</sup> Department of Physics, University of Liverpool, Liverpool, UK<sup>b</sup>  
<sup>19</sup> Queen Mary and Westfield College, London, UK<sup>b</sup>  
<sup>20</sup> Physics Department, University of Lund, Lund, Sweden<sup>g</sup>  
<sup>21</sup> Physics Department, University of Manchester, Manchester, UK<sup>b</sup>  
<sup>22</sup> CPPM, CNRS/IN2P3 - Univ Mediterranee, Marseille, France  
<sup>23</sup> Institute for Theoretical and Experimental Physics, Moscow, Russia  
<sup>24</sup> Lebedev Physical Institute, Moscow, Russia<sup>e,h</sup>  
<sup>25</sup> Max-Planck-Institut für Physik, München, Germany<sup>a</sup>  
<sup>26</sup> LAL, Université de Paris-Sud, IN2P3-CNRS, Orsay, France  
<sup>27</sup> LPNHE, Ecole Polytechnique, IN2P3-CNRS, Palaiseau, France  
<sup>28</sup> LPNHE, Universités Paris VI and VII, IN2P3-CNRS, Paris, France  
<sup>29</sup> Institute of Physics, Czech Academy of Sciences, Praha, Czech Republic<sup>e,i</sup>  
<sup>30</sup> Faculty of Mathematics and Physics, Charles University, Praha, Czech Republic<sup>e,i</sup>  
<sup>31</sup> Dipartimento di Fisica Università di Roma Tre and INFN Roma 3, Roma, Italy  
<sup>32</sup> Paul Scherrer Institut, Villigen, Switzerland  
<sup>33</sup> Fachbereich Physik, Bergische Universität Gesamthochschule Wuppertal, Wuppertal, Germany<sup>a</sup>  
<sup>34</sup> Yerevan Physics Institute, Yerevan, Armenia  
<sup>35</sup> DESY, Zeuthen, Germany<sup>a</sup>  
<sup>36</sup> Institut für Teilchenphysik, ETH, Zürich, Switzerland<sup>j</sup>  
<sup>37</sup> Physik-Institut der Universität Zürich, Zürich, Switzerland<sup>j</sup>  
<sup>38</sup> Also at Physics Department, National Technical University, Zografou Campus, GR-15773 Athens, Greece  
<sup>39</sup> Also at Rechenzentrum, Bergische Universität Gesamthochschule Wuppertal, Germany  
<sup>40</sup> Also at Institut für Experimentelle Kernphysik, Universität Karlsruhe, Karlsruhe, Germany  
<sup>41</sup> Also at Dept. Fis. Ap. CINVESTAV, Mérida, Yucatán, México<sup>k</sup>  
<sup>42</sup> Also at University of P.J. Šafárik, Košice, Slovak Republic  
<sup>43</sup> Also at CERN, Geneva, Switzerland

Received: 21 December 2000 / Published online: 6 April 2001 – © Springer-Verlag 2001

**Abstract.** A measurement is presented of dijet and 3-jet cross sections in low- $|t|$  diffractive deep-inelastic scattering interactions of the type  $ep \rightarrow eXY$ , where the system  $X$  is separated by a large rapidity gap from a low-mass baryonic system  $Y$ . Data taken with the H1 detector at HERA, corresponding to an integrated luminosity of  $18.0 \text{ pb}^{-1}$ , are used to measure hadron level single and double differential cross sections for  $4 < Q^2 < 80 \text{ GeV}^2$ ,  $x_{\mathbb{P}} < 0.05$  and  $p_{T,jet} > 4 \text{ GeV}$ . The energy flow not attributed to jets is also investigated. The measurements are consistent with a factorising diffractive exchange with trajectory intercept close to 1.2 and tightly constrain the dominating diffractive gluon distribution. Viewed in terms of the diffractive scattering of partonic fluctuations of the photon, the data require the dominance of  $q\bar{q}g$  over  $q\bar{q}$  states. Soft colour neutralisation models in their present form cannot simultaneously reproduce the shapes and the normalisations of the differential cross sections. Models based on 2-gluon exchange are able to reproduce the shapes of the cross sections at low  $x_{\mathbb{P}}$  values.

<sup>†</sup> Deceased

<sup>a</sup> Supported by the Bundesministerium für Bildung, Wissenschaft, Forschung und Technologie, FRG, under contract numbers 7AC17P, 7AC47P, 7DO55P, 7HH17I, 7HH27P, 7HD17P, 7HD27P, 7KI17I, 6MP17I and 7WT87P

<sup>b</sup> Supported by the UK Particle Physics and Astronomy Research Council, and formerly by the UK Science and Engineering Research Council

<sup>c</sup> Supported by FNRS-NFWO, IISN-IIKW

<sup>d</sup> Partially Supported by the Polish State Committee for

## 1 Introduction

The observation of deep-inelastic scattering (DIS) events at HERA containing a large gap in the rapidity distribution of the final state hadrons [1] has generated considerable renewed interest in understanding colour singlet exchange in strong interactions. At high energy, such interactions are interpreted as being due to diffractive scattering. HERA has made it possible to study diffraction using a highly virtual photon probe. This offers the chance to illuminate the underlying dynamics in terms of quantum chromodynamics (QCD).

Inclusive diffractive DIS is principally sensitive to the role of quarks in the scattering process [2–4]. More insight into the gluonic degrees of freedom can be obtained by studying the hadronic final state [5–8]. Final states containing heavy quarks or high transverse momentum ( $p_T$ ) jets are of particular interest, since the additional hard scales may ensure the applicability of perturbative QCD techniques [9–12]. High  $p_T$  jet production in diffraction has previously been studied both in  $p\bar{p}$  collisions [13–16] and at HERA [7, 8].

In this article, a high statistics measurement of diffractive jet production is presented, which was performed using the H1 detector. The data were obtained using events where the proton (or a low-mass proton excitation) loses only a small fraction of its incoming momentum and escapes undetected through the beam pipe. Separated from this system by a large rapidity region devoid of activity, the hadronic system  $X$  is well contained within the central part of the detector and contains the high  $p_T$  jets. The luminosity is increased by an order of magnitude compared with previous H1 measurements [8] and the kinematic range is also extended. This makes it possible to extract double differential cross sections for the first time and to study 3-jet as well as dijet production.

The dijet data yield direct constraints on the diffractive gluon distribution and are used to investigate the QCD [17] and Regge [18] factorisation properties of diffractive DIS. QCD inspired models [11, 12, 19] based on the exchange of a pair of gluons from the proton [20] are compared with the data in a restricted kinematic region where they are most likely to be applicable. Predictions from soft colour neutralisation models [21–23] are also confronted with the data.

The article is organised as follows. The kinematics of diffractive scattering at HERA are introduced in Sect. 2. In Sect. 3, an overview of phenomenological models and

Scientific Research, grant no. 2P0310318 and SPUB/DESY/P03/DZ-1/99, and by the German Federal Ministry of Education and Science, Research and Technology (BMBF)

<sup>e</sup> Supported by the Deutsche Forschungsgemeinschaft

<sup>f</sup> Supported by VEGA SR grant no. 2/5167/98

<sup>g</sup> Supported by the Swedish Natural Science Research Council

<sup>h</sup> Supported by Russian Foundation for Basic Research grant no. 96-02-00019

<sup>i</sup> Supported by GA AV ČR grant no. A1010821

<sup>j</sup> Supported by the Swiss National Science Foundation

<sup>k</sup> Supported by CONACyT

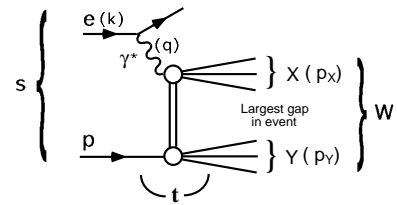


**Fig. 1.** The generic diffractive process at HERA, where the electron ( $k$ ) couples to a photon ( $q$ ) which interacts with the proton ( $P$ ) via net colour singlet exchange, producing two distinct final state hadronic systems  $X$  and  $Y$ . If the masses of  $X$  and  $Y$  are small compared with  $W$ , the two systems are separated by a large gap in rapidity

QCD calculations relevant for diffractive jet production is given and the Monte Carlo simulation of diffractive events is described. In Sect. 4, the data selection, the cross section measurement procedure and the determination of the systematic uncertainties are explained. The results, expressed in terms of hadron level single and double differential cross sections, are presented and discussed in Sect. 5.

## 2 Diffractive scattering at HERA

### 2.1 Inclusive diffractive scattering

Figure 1 illustrates the generic diffractive process at HERA of the type  $ep \rightarrow eXY$ . The electron<sup>1</sup> (with 4-momentum  $k$ ) couples to a virtual photon  $\gamma^*$  ( $q$ ) which interacts with the proton ( $P$ ). The usual DIS kinematic variables are defined as

$$Q^2 = -q^2; \quad y = \frac{P \cdot q}{P \cdot k}; \quad x = \frac{-q^2}{2P \cdot q}. \quad (1)$$

The squared invariant masses of the electron-proton and photon-proton systems  $s$  and  $W^2$  are given by

$$s = (k + P)^2 \simeq Q^2/xy \simeq (300 \text{ GeV})^2; \\ W^2 = (q + P)^2 \simeq ys - Q^2. \quad (2)$$

If the interaction takes place via colour singlet exchange, the photon and proton dissociate to produce distinct hadronic systems  $X$  and  $Y$ , with invariant masses  $M_X$  and  $M_Y$  respectively. In the case where  $M_X$  and  $M_Y$  are small compared with  $W$ , the two systems are separated by a large rapidity gap. The longitudinal momentum fraction  $x_P$  of the colourless exchange with respect to the incoming proton and the squared four-momentum transferred at the proton vertex  $t$  are then defined by

$$x_P = \frac{q \cdot (P - p_Y)}{q \cdot P}; \quad t = (P - p_Y)^2, \quad (3)$$

where  $p_Y$  is the 4-momentum of  $Y$ . In the analysis presented here,  $t$  and  $M_Y$  are not measured and hence are

<sup>1</sup> From now on, the word ‘electron’ will be used as a generic term for electrons and positrons

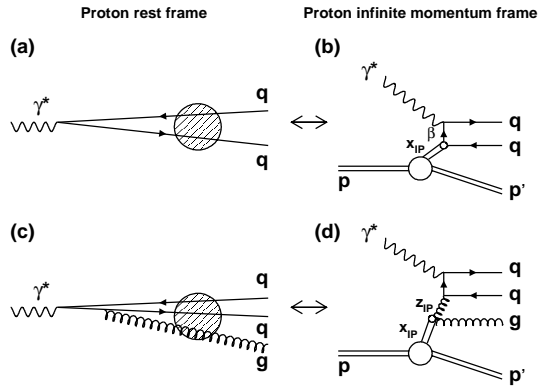


**Fig. 2a–d.** Diffractive scattering in the proton rest frame and the proton infinite momentum frame (figure after [21]). In the proton rest frame, the virtual photon dissociates into a  $q\bar{q}$  state **a**, scattering off the proton by colour singlet (e.g. 2-gluon) exchange. In the infinite momentum frame, this can be related to diffractive quark scattering **b**. The emission of an additional gluon forms an incoming  $q\bar{q}g$  state **c**. If the gluon is the lowest  $p_T$  parton, this contribution can be related to diffractive Boson-Gluon-Fusion **d**

integrated over implicitly<sup>2</sup>. In addition, the quantity  $\beta$  is defined as

$$\beta = \frac{x}{x_{\mathbb{P}}} = \frac{Q^2}{2q \cdot (P - p_Y)}. \quad (4)$$

In an interpretation in which partonic structure is ascribed to the colourless exchange,  $\beta$  is the longitudinal momentum fraction of the exchange that is carried by the struck quark, in analogy to  $x$  in the case of inclusive scattering.

## 2.2 Diffractive dijet production

Viewing DIS at low  $x$  in the proton rest frame, the virtual photon splits into a  $q\bar{q}$  pair well in advance of the proton target (Fig. 2a). The  $q\bar{q}$  state may then scatter elastically with the proton. The production of high  $p_T$  final states by the diffractive  $q\bar{q}$  scattering process is heavily suppressed [24] and the invariant masses  $M_X$  produced are typically small. It is thus expected that for large values of  $M_X$  or  $p_T$ ,  $\mathcal{O}(\alpha_s)$  contributions due to the radiation of an extra gluon become important [9, 25]. The result is an incoming  $q\bar{q}g$  system (Fig. 2c).

In the proton infinite momentum frame, the lowest order (i.e.  $\mathcal{O}(\alpha_s^0)$ ) contribution to the diffractive cross section is the quark scattering diagram (Fig. 2b). The  $\mathcal{O}(\alpha_s)$  contributions are Boson-Gluon-Fusion (BGF) and QCD-Compton (QCDC) scattering. Unlike inclusive diffractive scattering, jet production is directly sensitive to the role of gluons in diffraction due to the direct coupling to the gluon in the BGF diagram (Fig. 2d).

There is a correspondence between the proton rest frame and the infinite momentum frame pictures, which is discussed here in the context of the leading  $\log(Q^2)$  approximation. For the dominant configuration in which the

photon longitudinal momentum is shared asymmetrically between the partons, diffractive  $q\bar{q}$  scattering (Fig. 2a) can be related to the diffractive quark scattering diagram (Fig. 2b). If the gluon is the lowest  $p_T$  parton, the diffractive scattering of asymmetric  $q\bar{q}g$  configurations (Fig. 2c) can be related to diffractive BGF (Fig. 2d). If the  $q$  or  $\bar{q}$  is the lowest  $p_T$  parton, the process corresponds to diffractive QCDC scattering (not shown).

Using the non-zero invariant mass squared  $\hat{s}$  of the two highest  $p_T$  partons emerging from the hard interaction in the  $\mathcal{O}(\alpha_s)$  case, the quantity  $z_{\mathbb{P}}$  is introduced:

$$z_{\mathbb{P}} = \beta \cdot (1 + \hat{s}/Q^2). \quad (5)$$

Similarly to  $\beta$  for the case of the lowest order diagram (Fig. 2b),  $z_{\mathbb{P}}$  corresponds to the longitudinal momentum fraction of the exchange which takes part in the hard interaction (Fig. 2d).

## 3 Phenomenological models and Monte Carlo simulation

In this section, several phenomenological approaches and QCD calculations are discussed, which attempt to describe diffractive DIS, including diffractive jet production. The focus is on the models which are compared with the data in Sect. 5.

### 3.1 Diffractive parton distributions

In the leading  $\log(Q^2)$  approximation, the cross section for the diffractive process  $\gamma^* p \rightarrow p' X$  can be written in terms of convolutions of universal partonic cross sections  $\hat{\sigma}^{\gamma^* i}$  with diffractive parton distributions  $f_i^D$ , representing probability distributions for a parton  $i$  in the proton under the constraint that the proton remains intact with particular values of  $x_{\mathbb{P}}$  and  $t$ . Thus, at leading twist,

$$\frac{d^2\sigma(x, Q^2, x_{\mathbb{P}}, t)^{\gamma^* p \rightarrow p' X}}{dx_{\mathbb{P}} dt} = \sum_i \int_x^{x_{\mathbb{P}}} d\xi \hat{\sigma}^{\gamma^* i}(x, Q^2, \xi) f_i^D(\xi, Q^2, x_{\mathbb{P}}, t). \quad (6)$$

This factorisation formula holds for large enough  $Q^2$  and fixed  $x$ ,  $x_{\mathbb{P}}$  and  $t$ . This ansatz, introduced in [26, 27], was rigorously proven for inclusive diffractive lepton-hadron scattering in [28, 17]. The diffractive parton distributions are not known from first principles, though they should obey the DGLAP [29] evolution equations. Recently, there have been attempts to calculate the diffractive parton distributions at a starting scale  $\mu_0^2$  for QCD evolution under certain assumptions. In [30], the proton is replaced by a small-size pair of heavy quarks, such that perturbation theory can be applied. A different approach is the semi-classical model by Buchmüller, Gehrman and Hebecker [21], based on the opposite extreme of a very large hadron. In spite of the different assumptions, the two approaches

<sup>2</sup> It is noted that for this analysis  $M_Y = M_p$  dominantly

give rather similar results for the diffractive parton distributions. The general behaviour is the same as the momentum fractions tend to 0 or 1 and the gluon distribution dominates.

### 3.2 Resolved pomeron model and pomeron parton distributions

The application of Regge phenomenology of soft hadronic high energy interactions to the concept of diffractive parton distributions (Sect. 3.1) leads to the Ingelman-Schlein model of a ‘resolved pomeron’ with a partonic structure [18] invariant under changes in  $x_{\mathbb{P}}$  and  $t$ . The diffractive parton distributions then factorise into a flux factor  $f_{\mathbb{P}/p}$  and pomeron parton distributions  $f_i^{\mathbb{P}}$ :

$$f_i^D(x, Q^2, x_{\mathbb{P}}, t) = f_{\mathbb{P}/p}(x_{\mathbb{P}}, t) \cdot f_i^{\mathbb{P}}(\beta = x/x_{\mathbb{P}}, Q^2). \quad (7)$$

The universal flux factor describes the probability of finding a pomeron in the proton as a function of  $x_{\mathbb{P}}$  and  $t$ . The pomeron parton distributions are usually expressed in terms of  $\beta$ .

The triple differential cross section for inclusive diffraction  $d^3\sigma/d\beta dQ^2 dx_{\mathbb{P}}$  is often presented in the form of a diffractive structure function  $F_2^{D(3)}(\beta, Q^2, x_{\mathbb{P}})$ . In [3], the H1 collaboration interpreted a measurement of  $F_2^{D(3)}$  in terms of a resolved pomeron model: At the largest  $x_{\mathbb{P}}$  studied, it was necessary to consider more generally contributions from sub-leading reggeon exchanges<sup>3</sup> as well as the pomeron, such that (neglecting possible interference terms)

$$f_i^D(x, Q^2, x_{\mathbb{P}}, t) = f_{\mathbb{P}/p}(x_{\mathbb{P}}, t) \cdot f_i^{\mathbb{P}}(\beta, Q^2) + f_{\mathbb{R}/p}(x_{\mathbb{P}}, t) \cdot f_i^{\mathbb{R}}(\beta, Q^2). \quad (8)$$

The flux factors for the pomeron and reggeon exchanges were parameterised in a Regge-inspired form:

$$f_{\{\mathbb{P}, \mathbb{R}\}/p}(x_{\mathbb{P}}, t) = C_{\{\mathbb{P}, \mathbb{R}\}} x_{\mathbb{P}}^{1-2\alpha_{\{\mathbb{P}, \mathbb{R}\}}(t)} e^{b_{\{\mathbb{P}, \mathbb{R}\}}t}, \quad (9)$$

with  $\alpha_{\{\mathbb{P}, \mathbb{R}\}}(t) = \alpha_{\{\mathbb{P}, \mathbb{R}\}}(0) + \alpha'_{\{\mathbb{P}, \mathbb{R}\}}t$ . From fits in which the parton densities evolve according to the DGLAP equations, parameterisations of the pomeron quark and gluon distributions and values for the trajectory intercepts  $\alpha_{\mathbb{P}}(0)$  and  $\alpha_{\mathbb{R}}(0)$  were obtained. The resulting value of  $\alpha_{\mathbb{P}}(0) = 1.203 \pm 0.020$  (stat.)  $\pm 0.013$  (syst.)  $\pm 0.030$  (model) is significantly higher than that obtained from soft hadronic interactions, where  $\alpha_{\mathbb{P}}(0) \simeq 1.08$  [31]. The parton densities extracted for the pomeron are dominated by gluons, which carry 80 – 90% of the exchanged momentum throughout the measured  $Q^2$  range.

### 3.3 Colour dipole and 2-gluon exchange models

In the proton rest frame, diffractive DIS is often treated by considering the  $q\bar{q}$  and  $q\bar{q}g$  photon fluctuations (Fig. 2a,c)

<sup>3</sup> Throughout this paper, the term ‘reggeon’ ( $\mathbb{R}$ ) will be used to describe this contribution

as (effective) colour dipoles. The diffractive  $\gamma^*p$  cross section can be factorised into a squared effective photon dipole wave function and a squared ‘dipole cross section’ for the scattering of these dipoles off the proton [32,33]. The gross features of the diffractive  $\beta$  distribution can be deduced from a knowledge of the partonic wave functions of the photon alone. According to a recent QCD motivated parameterisation [34], longitudinally and transversely polarised  $q\bar{q}$  states dominate at high and medium values of  $\beta$  respectively, whereas the  $q\bar{q}g$  state originating from transversely polarised photons is dominant at low  $\beta$ .

Investigating diffractive final states with varying  $p_T$  probes the dipole cross section as a function of the dipole size. Large size, low  $p_T$  configurations interact with the proton similarly to soft hadron-hadron scattering. Small size, high  $p_T$  dipole configurations lead to hard scales which encourage a perturbative QCD treatment of the dipole cross section. The precise dynamics of the dipole cross section are not known a priori. However, the simplest realisation of a net colour singlet exchange at the parton level is a pair of gluons with cancelling colour charges [20]. We focus below on two recent colour dipole models [19, 11, 12] based on 2-gluon exchange, where the cross section is related to the square of the unintegrated gluon distribution of the proton  $\mathcal{F}(x, k_T^2)$  [35]. Here,  $k_T$  is the parton transverse momentum relative to the proton direction. Other colour dipole approaches can be found in [9, 10, 36].

The dipole approach has been employed in the ‘saturation’ model by Golec-Biernat and Wüsthoff [19]. Here, an ansatz for the dipole cross section is made which interpolates between the perturbative and non-perturbative regions of  $\sigma^{\gamma^*p}$ . This model is able to give a reasonable description of  $F_2(x, Q^2)$  at low  $x$ , which determines the three free parameters of the model. The parameterised dipole cross section can be re-expressed in terms of  $\mathcal{F}(x, k_T^2)$ , such that the diffractive cross section is predicted at  $t = 0$ . Introducing an additional free parameter  $B = 6.0 \text{ GeV}^{-2}$  to describe the  $t$  dependence as  $e^{Bt}$ , the diffractive structure function  $F_2^{D(3)}$  is successfully described. The calculation of the  $q\bar{q}g$  cross section is made under the assumption of strong  $k_T$  ordering of the final state partons (leading  $\log(Q^2)$  approximation), corresponding to  $k_T^{(g)} \ll k_T^{(q, \bar{q})}$ .

Cross sections for diffractive  $q\bar{q}$  and  $q\bar{q}g$  production by 2-gluon exchange have been calculated by Bartels, Ewerz, Lotter and Wüsthoff ( $q\bar{q}$ ) [11] and by Bartels, Jung, Kyrieleis and Wüsthoff ( $q\bar{q}g$ ) [12]. The derivative of the next-to-leading order (NLO) GRV gluon parameterisation [37] is used for  $\mathcal{F}(x, k_T^2)$ . The calculation of the  $q\bar{q}g$  final state is performed in the leading  $\log(1/\beta)$ , leading  $\log(1/x_{\mathbb{P}})$  approximation, such that configurations without strong  $k_T$  ordering are included. The calculations require all outgoing partons to have high  $p_T$  and are thus not suited to describe  $F_2^{D(3)}$ . The minimum value  $p_{T,g}^{\text{cut}}$  for the final state gluon transverse momentum is a free parameter which can be used to tune the model to the overall dijet cross section. As for the saturation model, the calculation yields predictions at  $t = 0$ . The extension to finite  $t$  is performed using the Donnachie-Landshoff elastic proton

form factor [38]. The sum of the  $q\bar{q}$  and  $q\bar{q}g$  contributions in this model is hereafter referred to as ‘BJLW’.

### 3.4 Soft colour neutralisation models

An alternative approach to diffractive DIS is given by soft colour neutralisation models, which naturally lead to very similar properties of inclusive and diffractive DIS final states. In the Soft Colour Interaction (SCI) model by Edin, Ingelman and Rathsman [22], the hard interaction in diffractive DIS is treated identically to that in inclusive DIS. Diffraction occurs through soft colour rearrangements between the outgoing partons, leaving their momentum configuration unchanged. If two colour singlet systems are produced by such a mechanism, the hadronic final state can exhibit a large rapidity gap. In the original SCI model, diffractive final states are produced using only one free parameter, the universal colour rearrangement probability, which is fixed by a fit to  $F_2^{D(3)}$ . The model has been refined recently [23] by making the colour rearrangement probability proportional to the normalised difference in the generalised areas of the string configurations before and after the rearrangement.

The semiclassical model, which was already mentioned in Sect. 3.1, is a non-perturbative model based on the dipole approach. Viewed in the proton rest frame,  $q\bar{q}$  and  $q\bar{q}g$  photon fluctuations scatter off a superposition of soft colour fields associated with the proton. Those configurations which emerge in a net colour singlet state contribute to the diffractive cross section [25]. Assuming a specific model for the proton wave functional [21], the results are formulated as a parameterisation of  $t$ -integrated diffractive parton distributions [39], which are determined from a combined four parameter fit to  $F_2$  and  $F_2^{D(3)}$  at low  $x$  and  $x_{\mathbb{P}}$ .

### 3.5 Monte Carlo simulation

Monte Carlo simulations are used to determine the corrections to be applied to the data to compensate for the limited efficiencies, acceptances and resolutions of the detector. The generated Monte Carlo events are passed through a detailed simulation of the H1 detector and are subjected to the same reconstruction and analysis chain as the data.

The main Monte Carlo generator used to correct the data is RAPGAP 2.08/06 [40]. Events are generated according to a resolved (partonic) pomeron model (Sect. 3.2). Contributions from pomeron and reggeon exchanges are included neglecting any possible interference effects. The parameterisations of the pomeron and reggeon parton distributions and flux factors (8 and 9) are taken from the H1 analysis of  $F_2^{D(3)}$  (see [3] and references therein). Explicitly the Regge trajectories and slope parameters are  $\alpha_{\mathbb{P}}(t) = 1.20 + 0.26t$ ,  $b_{\mathbb{P}} = 4.6 \text{ GeV}^{-2}$ ,  $\alpha_{\mathbb{R}}(t) = 0.50 + 0.90t$  and  $b_{\mathbb{R}} = 2.0 \text{ GeV}^{-2}$ . The chosen  $t$  dependences have negligible influence on the shape of the Monte Carlo event distributions as a function of  $x_{\mathbb{P}}$ ,  $\beta$  and

$Q^2$ . The pomeron parton distributions are taken from the ‘flat gluon’ (or ‘fit 2’ of [3]) solution in the leading order DGLAP fits to  $F_2^{D(3)}$ . Those of the meson are taken from fits to pion data [41]. The renormalisation and factorisation scales are set to  $\mu^2 = Q^2 + p_T^2$ , where  $p_T$  is the transverse momentum of the partons emerging from the hard scattering relative to the collision axis in the  $\gamma^*p$  centre-of-mass frame<sup>4</sup>. The parton distributions are convoluted with hard scattering matrix elements to  $\mathcal{O}(\alpha_s)$ . Intrinsic transverse momentum of the partons in the pomeron [42] is not included. Charm quarks are produced in the massive scheme via Boson-Gluon-Fusion. For the production of light quarks, a lower cut-off in  $p_T^2$  is introduced in the  $\mathcal{O}(\alpha_s)$  QCD matrix elements to avoid divergences. Higher order QCD diagrams are approximated with parton showers in the leading  $\log(Q^2)$  approximation (MEPS) [43] or the colour dipole approach<sup>5</sup> (CDM) [44] as implemented in ARIADNE [45]. Hadronisation is simulated using the Lund string model in JETSET [46]. QED radiative effects are taken into account via an interface to the HERACLES program [47].

The RAPGAP simulation includes a contribution of events where the virtual photon  $\gamma^*$  is assigned an internal partonic structure. The resolved virtual photon is parameterised according to the SaS-2D [48] set of photon parton densities, which has been found to give a reasonable description of inclusive dijet production at low  $Q^2$  [49].

Monte Carlo generators are also used to compare the measured hadron level cross sections with the predictions of the phenomenological models and QCD calculations described in Sects. 3.2-3.4. All of the predictions are made to leading order of QCD. Unless otherwise stated, higher order QCD effects are approximated by initial and final state parton showers. RAPGAP is used to obtain the predictions of the resolved pomeron model with different pomeron intercept values and parton distributions. It also contains implementations of the saturation, semiclassical and BJLW models. Both versions of the SCI model are implemented in the LEPTO 6.5.2 $\beta$  generator [50].

## 4 Experimental procedure

The analysis presented in this article is based on H1 data taken in the years 1996 and 1997, when HERA collided  $E_e = 27.5 \text{ GeV}$  positrons with protons of  $E_p = 820 \text{ GeV}$ . The data correspond to an integrated luminosity of  $18.0 \text{ pb}^{-1}$ . A detailed description of the measurement can be found in [51]. This section begins with a short overview of the H1 detector, after which the data selection is described. Then, the cross section measurement and the determination of the systematic errors are explained.

<sup>4</sup> This frame is also called the ‘hadronic centre-of-mass frame’

<sup>5</sup> ‘Colour dipole approach’ as an approximation to higher order QCD effects should not be confused with the ‘Colour dipole models’ introduced in Sect. 3.3

#### 4.1 H1 detector

The H1 detector is described in detail elsewhere [52]. Here, we give a brief description of the detector components most relevant for the present analysis. The  $z$  axis of the H1 coordinate system corresponds to the beam axis such that positive  $z$  values refer to the direction of the outgoing proton beam, often called the ‘forward’ direction<sup>6</sup>.

The interaction region is surrounded by the tracking system. Two large concentric drift chambers (CJC), located within a solenoidal magnetic field of 1.15 T, measure the trajectories of charged particles and hence their momenta in the range  $-1.5 < \eta < 1.5$ . The resolution is  $\sigma(p_T)/p_T \simeq 0.01p_T/\text{GeV}$ . Energies of final state particles are measured in a highly segmented Liquid Argon (LAr) calorimeter covering the range  $-1.5 < \eta < 3.4$ , surrounding the tracking detectors. The energy resolution is  $\sigma(E)/E \simeq 11\%/\sqrt{E/\text{GeV}}$  for electromagnetic showers and  $\sigma(E)/E \simeq 50\%/\sqrt{E/\text{GeV}}$  for hadrons, as obtained from test beam measurements. The overall hadronic energy scale of the LAr is known to 4%. The backward direction ( $-4.0 < \eta < -1.4$ ) is covered by a lead / scintillating fibre calorimeter (SPACAL) with electromagnetic and hadronic sections. The energy resolution for electrons is  $\sigma(E)/E \simeq 10\%/\sqrt{E/\text{GeV}}$ . The energy scale uncertainty is 0.3% for electrons with  $E'_e = 27.5$  GeV and 2.0% at  $E'_e = 8$  GeV. The electron polar angle is measured to 1 mrad. The energy scale of the SPACAL is known to 7% for hadrons. In front of the SPACAL, the Backward Drift Chamber (BDC) provides track segments of charged particles with a resolution of  $\sigma(r) = 0.4$  mm and  $r\sigma(\phi) = 0.8$  mm. The  $ep$  luminosity is determined with a precision of 2% by comparing the measured event rate in a photon tagger calorimeter close to the beam pipe at  $z = -103$  m with the QED Bremsstrahlung ( $ep \rightarrow ep\gamma$ ) cross section.

To enhance the sensitivity to hadronic activity in the region of the outgoing proton, the Forward Muon Detector (FMD) and the Proton Remnant Tagger (PRT) are used. The FMD is located at  $z = 6.5$  m and covers the pseudorapidity range  $1.9 < \eta < 3.7$  directly. Particles produced at larger  $\eta$  can also be detected because of secondary scattering with the beam-pipe. The PRT, a set of scintillators surrounding the beam pipe at  $z = 26$  m, can tag hadrons in the region  $6.0 \lesssim \eta \lesssim 7.5$ .

#### 4.2 Data selection

DIS events are triggered by an electromagnetic energy cluster in the SPACAL in coincidence with a CJC track. Scattered electron candidates are then selected with  $E'_e > 8$  GeV in the angular range  $156^\circ < \theta'_e < 176^\circ$ . Various cuts are applied on these candidates in order to select electrons and reject background from photons and hadrons. Among these are requirements on the width of the shower, the

containment within the electromagnetic part of the SPACAL and the existence of an associated track segment in the BDC. The  $z$  coordinate of the reconstructed vertex is required to lie within  $\pm 35$  cm ( $\pm \sim 3\sigma$ ) of the nominal interaction point. To suppress events with initial state QED radiation, the summed  $E - p_z$  of all reconstructed final state particles including the electron<sup>7</sup> has to be greater than 35 GeV. The DIS kinematic variables are calculated from the polar angle and energy measurements of the scattered electron:

$$Q^2 = 4E_e E'_e \cos^2 \frac{\theta'_e}{2}; \quad y = 1 - \frac{E'_e}{E_e} \sin^2 \frac{\theta'_e}{2}. \quad (10)$$

Events which fulfil  $4 < Q^2 < 80$  GeV<sup>2</sup> and  $0.1 < y < 0.7$  are selected.

The selection of diffractive events is based on the absence of hadronic activity in the outgoing proton region. No signal above noise levels is allowed in the FMD and PRT detectors. The most forward part ( $\eta > 3.2$ ) of the LAr calorimeter has to be devoid of hadronic clusters with energies  $E > 400$  MeV. This selection ensures that the photon dissociation system  $X$  is well contained within the central part of the H1 detector and is separated by a large rapidity gap covering at least  $3.2 < \eta \lesssim 7.5$  from the  $Y$  system. The upper limit in  $\eta$  implies that the  $Y$  system escapes undetected through the beam pipe and imposes the approximate constraint  $M_Y < 1.6$  GeV and  $|t| < 1.0$  GeV<sup>2</sup>.

The  $X$  system is measured in the LAr and SPACAL calorimeters together with the CJC. It is reconstructed using a method that combines calorimeter clusters and tracks whilst avoiding double counting [53]. The dissociation mass is then calculated according to

$$M_X^2 = (\sum_i E_i)^2 - (\sum_i \mathbf{p}_i)^2, \quad (11)$$

where the sum runs over all reconstructed objects except for the scattered electron<sup>8</sup>.  $W^2$  is calculated according to (2).  $x_{\mathbb{P}}$  and  $\beta$  are then computed from

$$x_{\mathbb{P}} = \frac{Q^2 + M_X^2}{Q^2 + W^2}; \quad \beta = \frac{Q^2}{Q^2 + M_X^2}. \quad (12)$$

A cut  $x_{\mathbb{P}} < 0.05$  is applied to suppress contributions from non-diffractive scattering and secondary exchanges. The resolution in  $\log x_{\mathbb{P}}$  is approximately 8%.

The 4-vectors of the hadronic final state particles associated to the  $X$  system are Lorentz-transformed to the  $\gamma^*p$  centre-of-mass frame, where they are subjected to the CDF cone jet algorithm [54] with a cone radius of  $\sqrt{(\Delta\eta)^2 + (\Delta\phi)^2} = 1.0$ . The jets are required to lie within the region  $-1.0 < \eta_{jet}^{lab} < 2.2$  to ensure good containment within the LAr calorimeter. Transverse energies and momenta are calculated with respect to the  $\gamma^*p$  axis. Events

<sup>7</sup> For events fully contained in the detector, the total  $E - p_z$  is sharply peaked at  $2E_e = 55$  GeV

<sup>8</sup> When calculating all hadronic final state quantities, particle masses are neglected

<sup>6</sup> This direction corresponds to positive values of the pseudorapidity  $\eta = -\ln \tan \theta/2$

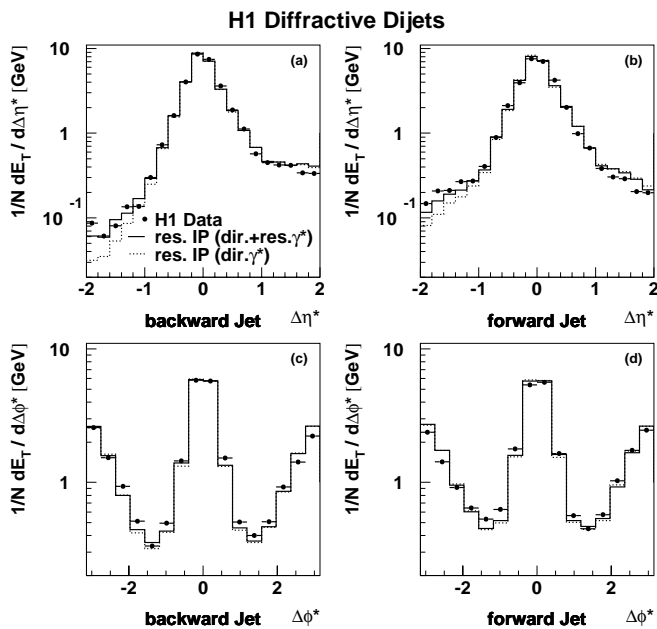


**Fig. 3a–d.** Observed distributions of the average transverse energy flow per event around the jet axes in the diffractive dijet sample.  $\Delta\eta^*$  and  $\Delta\phi^*$  are the distances from the jet axes in pseudorapidity and azimuthal angle in the hadronic centre-of-mass frame. The jet profiles in  $\eta$  and  $\phi$  are integrated over  $\pm 1$  unit in  $\phi$  and  $\eta$  respectively. **a** and **c** show the distributions for the backward jet in the laboratory frame, whereas **b** and **d** show those for the forward jet. The distributions for the simulated sample of RAPGAP events are compared with the data. Here, the contributions from direct photons only (*dotted histograms*) and from the sum of direct and resolved photon contributions (*solid histograms*) are shown

with either at least two or exactly three jets with transverse momentum  $p_{T,jet}^* > 4$  GeV are selected for the dijet and 3-jet samples respectively. The average resolution in  $p_{T,jet}^*$  is 14%. No requirements are made on the presence or absence of hadronic activity beyond the jets. The final event selection yields 2506 dijet and 130 3-jet events.

Figure 3 shows the transverse energy flow around the jet axes for the dijet sample. For the jet profiles in  $\eta$  and  $\phi$ , only transverse energies within one unit in azimuth and pseudorapidity are included in the plots respectively. The jet profiles for backward and forward jets are shown separately in Figs. 3a,c and b,d. The data exhibit a clear back-to-back dijet structure in azimuth. The energy flow is well described by the RAPGAP simulation that is used to correct the data (solid lines).

### 4.3 Cross section measurement

The data are first corrected for losses at the trigger level, which occur due to the track requirement. For the selected events, the trigger efficiency varies between 80 and 90%, depending on the kinematics. Corrections for detector acceptances and migrations between measurement intervals are evaluated by applying a bin-to-bin correction method

**Table 1.** The kinematic range to which the dijet and 3-jet hadron level cross sections are corrected. The details of the jet finding algorithm can be found in Sect. 4.2

Kinematic Range of Hadron Level Cross Sections
$4 < Q^2 < 80 \text{ GeV}^2$
$0.1 < y < 0.7$
$x_P < 0.05$
$M_Y < 1.6 \text{ GeV}$
$ t  < 1.0 \text{ GeV}^2$
$N_{jets} \geq 2$ or $N_{jets} = 3$
$p_{T,jet}^* > 4 \text{ GeV}$
$-3 < \eta_{jet}^* < 0$

using the RAPGAP program (see Sect. 3.5). The simulation gives an acceptable description of all relevant kinematic distributions of the selected dijet and 3-jet events. Smearing in  $x_P$  is taken into account up to  $x_P = 0.2$  by the simulation of colour-singlet exchange in RAPGAP. Migrations from  $x_P > 0.2$  or from large values of  $M_Y > 5$  GeV are covered by a RAPGAP simulation of inclusive DIS. This contribution is at the level of 5% averaged over all measured bins and is concentrated at large  $x_P$ . An additional correction of  $-6.5\% \pm 6.5\%$  is applied to account for the net smearing about the  $M_Y = 1.6$  GeV boundary. Since only elastically scattered protons have been simulated in RAPGAP, this correction is evaluated using the proton dissociation simulation in the DIFFVM [55] Monte Carlo model. A further correction of  $+5.5\% \pm 1.4\%$  takes into account diffractive events rejected due to fluctuations in the noise level in the FMD. This correction is determined using randomly triggered events. QED radiative corrections are of the order of 5%. The bin purities and stabilities<sup>9</sup> are typically of the order of 50 to 60% and it is ensured that they exceed 30% for every measured data point.

The corrected cross sections are defined in a model-independent manner, whereby the systems  $X$  and  $Y$  are separated by the largest gap in rapidity among the hadrons in the  $\gamma^*p$  centre-of-mass frame (Fig. 1). The  $ep$  cross sections are corrected to the hadron level and are quoted at the Born level. The kinematic range in which the cross sections are measured is fully specified in Table 1. The measured range of jet pseudorapidities in the hadronic centre-of-mass frame  $-3 < \eta_{jet}^* < 0$  approximately matches the  $-1 < \eta_{jet}^{lab} < 2.2$  cut for the selected events. No  $\eta_{max}$  or similar cuts are imposed in the definition of the measured cross sections.

<sup>9</sup> ‘Bin purity’ is defined as the fraction of simulated events reconstructed in a bin that are also generated in that bin. ‘Stability’ is the fraction of events generated in a bin that are also reconstructed in that bin

#### 4.4 Analysis of systematic uncertainties

The following sources of uncertainty contribute to the systematic errors on the measured cross sections. The uncertainties associated with detector understanding (see Sect. 4.1) are as follows.

1. The uncertainties in the hadronic calibrations of the LAr and SPACAL calorimeters mainly influence the measured values of  $p_{T,jet}^*$  and  $M_X$ . The resulting uncertainties in the cross sections are up to 10% (with a mean value of 5%) for the LAr and 0.5% for the SPACAL.
2. The uncertainties in the  $E'_e$  and  $\theta'_e$  measurements propagate into the reconstruction of  $Q^2$ ,  $y$  and  $W$  and the definition of the  $\gamma^*p$  axis for the boost into the  $\gamma^*p$  centre-of-mass frame. The uncertainty in  $\theta'_e$  leads to a systematic error of 1% to 2%. The uncertainty in  $E'_e$  results in a systematic error between 1% and 5%, depending on the kinematics.
3. The uncertainty in the fraction of energy of the reconstructed hadronic objects carried by tracks is 3%, leading to a systematic error in the range 1% to 5%.
4. The uncertainties in the determinations of the trigger efficiency and the  $ep$  luminosity affect the total normalisation by 5% and 2% respectively.
5. There is an uncertainty of 25% in the fraction of events lost due to noise in the FMD, which translates into a 1.4% normalisation error on the measured cross sections.

The Monte Carlo modelling of the data gives rise to the following uncertainties.

6. The uncertainty in the number of events migrating into the sample from  $x_{\mathbb{P}} > 0.2$  or  $M_Y > 5$  GeV is estimated as 25%, leading to a systematic error between 1% and 3%, with the biggest values at large  $x_{\mathbb{P}}$ .
7. A 6.5% uncertainty arises from the correction for smearing about the  $M_Y$  limit of the measurement. It is estimated by variations of: (a) the ratio of elastic proton to proton dissociation cross sections in DIFFVM between 1:2 and 2:1; (b) the generated  $M_Y$  distribution within  $1/M_Y^{2.0\pm 0.3}$ ; (c) the  $t$  dependencies in the proton dissociation simulation by changing the slope parameter by  $\pm 1$  GeV $^{-2}$  and (d) the simulated efficiencies of the forward detectors FMD and PRT by  $\pm 4\%$  and  $\pm 25\%$  respectively.
8. The uncertainty arising from the QED radiative corrections is typically 5%, originating from the limited statistics of the Monte Carlo event samples.
9. The use of different approximations for higher order QCD diagrams (the parton shower (MEPS) model or the colour dipole (CDM) approach) leads to a 3% uncertainty in the cross sections.
10. The model dependence of the acceptance and migration corrections obtained from the RAPGAP simulation is estimated by varying the shapes of kinematic distributions in the simulations beyond the limits imposed by previous measurements or the present data. This is done by reweighting (a) the  $z_{\mathbb{P}}$  distribution

by  $z_{\mathbb{P}}^{\pm 0.2}$  and  $(1 - z_{\mathbb{P}})^{\pm 0.2}$ ; (b) the  $p_T$  distribution by  $(1/p_T)^{\pm 0.5}$ ; (c) the  $x_{\mathbb{P}}$  distribution by  $(1/x_{\mathbb{P}})^{\pm 0.2}$ ; (d) the  $t$  distribution by  $e^{\pm 2t}$  and (e) the  $\eta_{jet}^{lab}$  distribution to that observed in the data. The resulting systematic uncertainties range between 6% and 13%, the largest contributions originating from (c) and (e).

11. The lower  $p_T^2$ -cut-off chosen to avoid collinear divergences in the leading order QCD matrix elements in RAPGAP is relatively high ( $p_T^2 > 9$  GeV $^2$ ) with respect to the experimental cut of  $p_{T,jet}^{*2} > 16$  GeV $^2$ . Studying the dependence on the cut-off value results in an additional uncertainty of 5%.

Most of the systematic uncertainties are not strongly correlated between data points. The total systematic error has been evaluated for each data point by adding all individual systematic errors in quadrature. It ranges between 15 and 30% and for most data points is significantly larger than the statistical uncertainty.

## 5 Results

In this section, the measured hadron level differential cross sections are presented for the kinematic region specified in Table 1. The cross sections are shown graphically in Figs. 5–12. In all figures, the inner error bars correspond to the statistical error, whilst the outer error bars represent the quadratic sum of the statistical and systematic errors. The numerical values of the measured cross sections can be found in Table s2–7. The quoted differential cross sections are average values over the intervals specified in the tables.

### 5.1 General properties of the dijet data

In this section, general features of the data are discussed, referring to Figs. 4–7. The model predictions<sup>10</sup> which are also shown in these figures are discussed in Sects. 5.2 and 5.3.

In Fig. 4a, the uncorrected average transverse energy flow per event for the dijet sample is shown as a function of the pseudorapidity  $\eta^\dagger$  in the rest frame of the  $X$  system<sup>11</sup>. Positive values of  $\eta^\dagger$  correspond to the pomeron hemisphere, negative values to the photon hemisphere. Both the total energy flow and the energy flow from particles outside the two leading jets are shown. The data exhibit considerable hadronic energy not associated with the jets. This additional energy is distributed in both hemispheres with some preference for the pomeron hemisphere. In order to examine the sharing of energy within the  $X$  system on an event-by-event basis, Fig. 4b shows the uncorrected correlation between the squared dijet invariant mass  $M_{12}^2$

<sup>10</sup> Software to produce predictions for the measured cross sections using any hadron level  $ep$  Monte Carlo model is available in the HZTOOL package [56]

<sup>11</sup> This frame can be interpreted as the  $\gamma^*\mathbb{P}$  centre-of-mass frame. In this context, ‘ $\mathbb{P}$ ’ or ‘pomeron’ is used synonymously with ‘colourless exchange’

**Table 2.** Differential hadron level dijet cross sections. Here and elsewhere, the quoted differential cross sections are average values over the specified intervals

Dijet cross section as a function of $Q^2$ .							
Bin	$Q^2$ [GeV <sup>2</sup> ]		$\sigma$ [pb/GeV <sup>2</sup> ]	stat. err. [%]	syst. err. [%]	tot. err. [%]	
1	4.0	– 6.0	21.4	4.5	16.4	17.0	
2	6.0	– 10.0	13.0	4.0	16.1	16.6	
3	10.0	– 15.0	6.3	4.8	17.0	17.7	
4	15.0	– 20.0	4.1	6.2	16.7	17.8	
5	20.0	– 30.0	2.3	5.8	16.4	17.4	
6	30.0	– 40.0	1.2	8.0	16.3	18.2	
7	40.0	– 50.0	0.7	10.4	19.7	22.3	
8	50.0	– 60.0	0.7	12.5	23.9	27.0	
9	60.0	– 80.0	0.4	11.9	29.6	31.9	

Dijet cross section as a function of $p_{T,jets}^*$ .							
Bin	$p_{T,jets}^*$ [GeV]		$\sigma$ [pb/GeV]	stat. err. [%]	syst. err. [%]	tot. err. [%]	
1	4.0	– 5.0	74.9	4.0	17.8	18.3	
2	5.0	– 6.0	59.5	3.3	16.4	16.8	
3	6.0	– 7.5	28.8	3.9	17.3	17.8	
4	7.5	– 9.0	9.9	7.0	17.9	19.2	
5	9.0	– 11.0	3.4	11.0	17.7	20.8	
6	11.0	– 14.0	0.9	18.9	18.6	26.5	

Dijet cross section as a function of $\langle\eta\rangle_{jets}^{lab}$ .							
Bin	$\langle\eta\rangle_{jets}^{lab}$		$\sigma$ [pb]	stat. err. [%]	syst. err. [%]	tot. err. [%]	
1	–1.00	– –0.66	22.4	13.5	34.3	36.9	
2	–0.66	– –0.33	68.9	6.3	17.7	18.8	
3	–0.33	– 0.00	112.8	4.7	15.7	16.4	
4	0.00	– 0.33	131.6	4.2	15.7	16.3	
5	0.33	– 0.66	127.9	4.3	17.5	18.0	
6	0.66	– 1.00	85.3	5.1	17.4	18.2	
7	1.00	– 1.50	16.4	6.8	25.6	26.5	

Dijet cross section as a function of $M_X$ .							
Bin	$M_X$ [GeV]		$\sigma$ [pb/GeV]	stat. err. [%]	syst. err. [%]	tot. err. [%]	
1	8.0	– 14.0	1.9	10.1	20.0	22.4	
2	14.0	– 20.0	7.5	4.4	15.1	15.7	
3	20.0	– 30.0	7.3	3.2	16.9	17.2	
4	30.0	– 40.0	4.5	4.0	17.8	18.3	
5	40.0	– 60.0	1.2	6.2	27.1	27.8	

Dijet cross section as a function of $W$ .							
Bin	$W$ [GeV]		$\sigma$ [pb/GeV]	stat. err. [%]	syst. err. [%]	tot. err. [%]	
1	90.0	– 115.0	1.1	6.6	20.3	21.3	
2	115.0	– 140.0	1.4	5.1	18.5	19.2	
3	140.0	– 165.0	1.7	4.4	18.0	18.5	
4	165.0	– 190.0	1.3	4.5	17.7	18.3	
5	190.0	– 215.0	1.1	4.7	17.7	18.3	
6	215.0	– 240.0	0.9	5.4	17.0	17.8	
7	240.0	– 260.0	0.5	10.3	28.5	30.3	

and the squared total diffractive mass  $M_X^2$  [25].  $M_{12}$  is calculated from the massless jet 4-vectors. Except for a small subset of the events at low  $M_X$ , only a fraction of the available energy of the  $X$  system is contained in the dijet system, such that  $M_{12}$  is considerably smaller than  $M_X$  on average.

Figures 5 and 6 present differential dijet cross sections as functions of the following observables: the photon virtuality  $Q^2$ ; the mean dijet transverse momentum  $p_{T,jets}^*$ , defined as

$$p_{T,jets}^* = \frac{1}{2} (p_{T,jet 1}^* + p_{T,jet 2}^*) ; \quad (13)$$

**Table 3.** Differential hadron level dijet cross sections (continued)

Dijet cross section as a function of $\log_{10} x_{\mathbb{P}}$ .							
Bin	$\log_{10} x_{\mathbb{P}}$		$\sigma$ [pb]	stat. err. [%]	syst. err. [%]	tot. err. [%]	
1	-2.5	-	-2.3	7.3	21.8	28.8	36.1
2	-2.3	-	-2.1	35.4	10.8	25.1	27.4
3	-2.1	-	-1.9	88.2	6.8	17.5	18.8
4	-1.9	-	-1.7	171.2	4.7	16.3	17.0
5	-1.7	-	-1.5	269.3	3.6	16.3	16.7
6	-1.5	-	-1.3	440.7	3.2	18.6	18.8
Dijet cross section as a function of $\log_{10} \beta$ .							
Bin	$\log_{10} \beta$		$\sigma$ [pb]	stat. err. [%]	syst. err. [%]	tot. err. [%]	
1	-2.8	-	-2.5	24.9	11.3	26.4	28.7
2	-2.5	-	-2.2	88.3	5.6	18.1	19.0
3	-2.2	-	-1.9	129.9	4.3	16.7	17.2
4	-1.9	-	-1.6	152.7	3.9	17.4	17.9
5	-1.6	-	-1.3	145.9	4.3	16.8	17.3
6	-1.3	-	-1.1	85.0	7.0	17.5	18.8
7	-1.1	-	-0.8	53.4	7.8	17.4	19.0
8	-0.8	-	-0.5	13.5	17.7	29.8	34.6
Dijet cross section as a function of $z_{\mathbb{P}}^{(jets)}$ .							
Bin	$z_{\mathbb{P}}^{(jets)}$		$\sigma$ [pb]	stat. err. [%]	syst. err. [%]	tot. err. [%]	
1	0.000	-	0.125	269.4	5.8	23.7	24.4
2	0.125	-	0.250	493.9	3.8	18.4	18.8
3	0.250	-	0.375	331.3	4.2	18.6	19.1
4	0.375	-	0.500	233.2	4.9	18.5	19.2
5	0.500	-	0.625	174.2	5.9	16.1	17.2
6	0.625	-	0.750	94.0	8.1	16.3	18.2
7	0.750	-	0.875	39.8	11.7	16.3	20.0
8	0.875	-	1.000	30.0	16.7	24.5	29.7
Dijet cross section as a function of $x_{\gamma}^{(jets)}$ .							
Bin	$x_{\gamma}^{(jets)}$		$\sigma$ [pb]	stat. err. [%]	syst. err. [%]	tot. err. [%]	
1	0.0	-	0.2	25.4	14.3	35.1	37.9
2	0.2	-	0.4	104.8	6.5	17.7	18.9
3	0.4	-	0.6	153.8	5.0	18.1	18.8
4	0.6	-	0.8	331.5	3.6	18.0	18.3
5	0.8	-	1.0	428.3	3.1	16.7	17.0
Dijet cross section as a function of $E_{rem}^{(\gamma)}$ .							
Bin	$E_{rem}^{(\gamma)}$ [GeV]		$\sigma$ [pb/GeV]	stat. err. [%]	syst. err. [%]	tot. err. [%]	
1	0.0	-	4.0	38.1	2.5	17.2	17.3
2	4.0	-	8.0	9.0	4.7	17.6	18.2
3	8.0	-	12.0	4.0	6.7	25.4	26.3
4	12.0	-	20.0	2.0	8.0	38.6	39.4

the  $\gamma^*p$  invariant mass  $W$ ; the mean dijet pseudorapidity in the laboratory frame  $\langle \eta \rangle_{jets}^{lab}$ , defined as

$$\langle \eta \rangle_{jets}^{lab} = \frac{1}{2} (\eta_{jet1}^{lab} + \eta_{jet2}^{lab}) ; \quad (14)$$

and the logarithms of the  $x_{\mathbb{P}}$  and  $\beta$  variables. The  $Q^2$  and  $p_{T,jets}^*$  distributions are steeply falling. Due to the selection of events with  $Q^2 > 4$  GeV<sup>2</sup> and  $p_{T,jets}^{*2} > 16$  GeV<sup>2</sup>, the relation  $p_{T,jets}^{*2} > Q^2$  holds for the bulk of the data. As can be seen in Fig. 5c, the  $W$  range of the selected events is approximately  $90 < W < 260$  GeV. The  $x_{\mathbb{P}}$  distribution

shows a rising behaviour from the lowest accessible values of  $\sim 0.003$  up to the cut value of 0.05. For kinematic reasons, the dijet measurement is dominated by larger  $x_{\mathbb{P}}$  values than is the case for inclusive diffractive measurements. The  $\beta$  range covered by the measurement extends down to almost  $10^{-3}$ , lower than accessed so far in measurements of  $F_2^{D(3)}$ . The shapes of the measured cross sections are generally well described by the RAPGAP simulation used to correct the data (solid histograms), except for the  $\langle \eta \rangle_{jets}^{lab}$  distribution, which shows that on average the

**Table 4.** Differential hadron level dijet cross sections in four bins of  $\log_{10} x_{\mathbb{P}}$ 

Dijet cross section as a function of $z_{\mathbb{P}}^{(jets)}$ for $-1.5 < \log_{10} x_{\mathbb{P}} < -1.3$ .							
Bin	$z_{\mathbb{P}}^{(jets)}$		$\sigma$ [pb]	stat. err. [%]	syst. err. [%]	tot. err. [%]	
1	0.00	–	0.15	232.9	6.0	29.7	30.3
2	0.15	–	0.30	209.4	5.3	24.2	24.8
3	0.30	–	0.50	85.4	6.4	20.8	21.8
4	0.50	–	0.70	30.9	10.4	18.8	21.5
5	0.70	–	1.00	3.4	28.9	47.0	55.1
Dijet cross section as a function of $z_{\mathbb{P}}^{(jets)}$ for $-1.75 < \log_{10} x_{\mathbb{P}} < -1.5$ .							
Bin	$z_{\mathbb{P}}^{(jets)}$		$\sigma$ [pb]	stat. err. [%]	syst. err. [%]	tot. err. [%]	
1	0.0	–	0.2	97.1	6.4	20.8	21.8
2	0.2	–	0.4	134.3	5.3	19.0	19.7
3	0.4	–	0.6	63.4	7.1	16.3	17.7
4	0.6	–	0.8	21.8	12.6	16.6	20.8
5	0.8	–	1.0	8.5	25.8	34.4	43.0
Dijet cross section as a function of $z_{\mathbb{P}}^{(jets)}$ for $-2.0 < \log_{10} x_{\mathbb{P}} < -1.75$ .							
Bin	$z_{\mathbb{P}}^{(jets)}$		$\sigma$ [pb]	stat. err. [%]	syst. err. [%]	tot. err. [%]	
1	0.00	–	0.30	37.8	8.3	23.4	24.9
2	0.30	–	0.45	59.7	9.2	18.2	20.4
3	0.45	–	0.60	49.1	11.2	19.4	22.4
4	0.60	–	0.80	33.8	10.9	19.1	22.0
5	0.80	–	1.00	9.0	21.8	24.8	33.0
Dijet cross section as a function of $z_{\mathbb{P}}^{(jets)}$ for $\log_{10} x_{\mathbb{P}} < -2.0$ .							
Bin	$z_{\mathbb{P}}^{(jets)}$		$\sigma$ [pb]	stat. err. [%]	syst. err. [%]	tot. err. [%]	
1	0.00	–	0.30	5.2	30.2	85.2	90.4
2	0.30	–	0.45	25.8	16.2	31.5	35.4
3	0.45	–	0.60	28.0	13.9	21.3	25.5
4	0.60	–	0.80	24.8	12.8	18.9	22.9
5	0.80	–	1.00	11.9	17.4	22.0	28.0

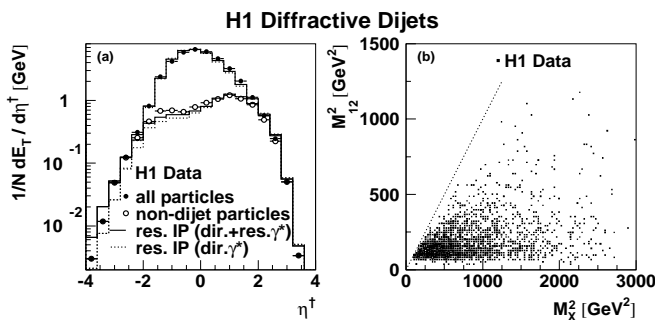


**Fig. 4.** **a** The uncorrected distribution of the average transverse energy per event for the diffractive dijet sample as a function of the pseudorapidity  $\eta^\dagger$  in the centre-of-mass frame of the X system. Distributions are shown both for all final state particles (*solid points*) and for only those particles which do not belong to the two highest  $p_T$  jets (*open points*). The prediction of the RAPGAP simulations for direct and for direct plus resolved virtual photon contributions are also shown. **b** The uncorrected correlation between the squared invariant mass of the X system  $M_X^2$  and the squared dijet invariant mass  $M_{12}^2$  for the diffractive dijet sample. The dotted line corresponds to  $M_X^2 = M_{12}^2$

measured jets have slightly larger pseudorapidities than is predicted by the simulations.

In Fig. 7, the cross section is shown differentially in  $z_{\mathbb{P}}^{(jets)}$ , which is calculated from

$$z_{\mathbb{P}}^{(jets)} = \frac{Q^2 + M_{12}^2}{Q^2 + M_X^2}. \quad (15)$$

Monte Carlo studies show that the resolution in  $z_{\mathbb{P}}^{(jets)}$  is approximately 25% and that there is a good correlation between  $z_{\mathbb{P}}^{(jets)}$  and the value of  $z_{\mathbb{P}}$  as defined at the parton level in 5. In loose terms, the  $z_{\mathbb{P}}^{(jets)}$  observable measures the fraction of the hadronic final state energy of the X system which is contained in the two jets. The measured  $z_{\mathbb{P}}^{(jets)}$  distribution is largest around 0.2 and thus confirms the observation from Fig. 4 that the total energy of the X system is typically much larger than that contained in the jets. Diffractively scattered  $q\bar{q}$  photon fluctuations (see Sect. 2.2) satisfy  $z_{\mathbb{P}} \equiv 1$  at the parton level, but can be smeared to  $z_{\mathbb{P}}^{(jets)}$  values as low as 0.6 because of fragmentation and jet resolution effects. Even taking this smearing into account, the  $z_{\mathbb{P}}^{(jets)}$  distribution implies

**Table 5.** Differential hadron level dijet cross sections in four bins of  $Q^2 + p_T^2$ .  
Dijet cross section as a function of  $z_{\mathbb{P}}^{(jets)}$  for  $20 \text{ GeV}^2 < Q^2 + p_T^2 < 35 \text{ GeV}^2$ .

Bin	$z_{\mathbb{P}}^{(jets)}$			$\sigma$ [pb]	stat. err. [%]	syst. err. [%]	tot. err. [%]
1	0.0	–	0.2	150.5	6.7	32.4	33.1
2	0.2	–	0.4	109.0	7.3	26.6	27.6
3	0.4	–	0.6	45.2	10.8	28.8	30.8
4	0.6	–	0.8	18.7	16.2	31.6	35.5
5	0.8	–	1.0	5.9	31.6	54.4	63.0

Dijet cross section as a function of  $z_{\mathbb{P}}^{(jets)}$  for  $35 \text{ GeV}^2 < Q^2 + p_T^2 < 45 \text{ GeV}^2$ .

Bin	$z_{\mathbb{P}}^{(jets)}$			$\sigma$ [pb]	stat. err. [%]	syst. err. [%]	tot. err. [%]
1	0.0	–	0.2	89.7	7.1	25.2	26.2
2	0.2	–	0.4	71.8	6.9	21.8	22.9
3	0.4	–	0.6	39.3	9.0	26.1	27.6
4	0.6	–	0.8	16.9	14.4	26.3	30.0
5	0.8	–	1.0	4.3	27.7	26.2	38.1

Dijet cross section as a function of  $z_{\mathbb{P}}^{(jets)}$  for  $45 \text{ GeV}^2 < Q^2 + p_T^2 < 60 \text{ GeV}^2$ .

Bin	$z_{\mathbb{P}}^{(jets)}$			$\sigma$ [pb]	stat. err. [%]	syst. err. [%]	tot. err. [%]
1	0.0	–	0.2	74.6	7.7	24.6	25.8
2	0.2	–	0.4	78.0	6.7	24.5	25.4
3	0.4	–	0.6	43.2	8.6	18.6	20.5
4	0.6	–	0.8	14.7	14.7	20.1	25.0
5	0.8	–	1.0	5.5	23.6	28.7	37.2

Dijet cross section as a function of  $z_{\mathbb{P}}^{(jets)}$  for  $Q^2 + p_T^2 > 60 \text{ GeV}^2$ .

Bin	$z_{\mathbb{P}}^{(jets)}$			$\sigma$ [pb]	stat. err. [%]	syst. err. [%]	tot. err. [%]
1	0.0	–	0.2	58.7	9.2	25.2	26.9
2	0.2	–	0.4	114.6	5.8	17.4	18.4
3	0.4	–	0.6	73.4	6.8	15.6	17.0
4	0.6	–	0.8	45.3	9.4	15.3	18.0
5	0.8	–	1.0	14.4	18.3	22.3	28.8

the dominance of  $q\bar{q}g$  over  $q\bar{q}$  scattering in the proton rest frame picture.

## 5.2 Interpretation within a partonic pomeron model

In this section, the data are compared with the Ingelman-Schlein model (Sect.3.2), using the RAPGAP Monte Carlo model with various sets of pomeron parton distributions. In all cases unless otherwise stated, the RAPGAP predictions shown use the parton shower approximation to higher order diagrams (MEPS) and a contribution from resolved virtual photons is included, as described in Sect.3.5. It has been shown in an H1 measurement of inclusive dijet production for similar ranges in  $Q^2$  and  $p_{T,jets}^*$  [49] that including resolved photon contributions improves the description of the data by leading order Monte Carlo Models in the region  $p_{T,jets}^* > Q^2$ . It is thus reasonable to expect a similar contribution in diffraction.

### 5.2.1 Diffractive gluon distribution

Pomeron parton densities dominated by gluons have proved successful in describing not only inclusive mea-

surements of the diffractive structure function [2–4], but also more exclusive hadronic final state analyses [5–8]. By contrast, pomeron parton distributions dominated by quarks (e.g. ‘fit 1’ from [3]) do not describe the data [3, 8, 5]. In particular, they lead to significantly smaller predicted dijet electroproduction cross sections than were obtained in previous measurements [8]. The free parameters of the Ingelman-Schlein model to which dijet production is most sensitive are the pomeron gluon distribution  $g_{\mathbb{P}}(z, \mu^2)$  and the pomeron intercept  $\alpha_{\mathbb{P}}(0)$ . The sub-leading reggeon contribution and the pomeron quark distribution are better constrained by inclusive colour singlet exchange measurements [3, 57].

Predictions based on two sets of pomeron parton distributions obtained from the leading order DGLAP analysis of  $F_2^{D(3)}$  from H1 in [3] are compared with the data in Figs. 5, 6. The ‘flat gluon’ or ‘fit 2’ parameterisation gives a very good description of all differential distributions, except for  $d\sigma/d\langle\eta\rangle_{jets}^{lab}$ . The predictions based on the ‘peaked gluon’ or ‘fit 3’ parameterisation in Figs. 5, 6 are also in fair agreement with the data, though the description is somewhat poorer than that from ‘fit 2’. If the colour dipole approximation (CDM) to higher order QCD effects is used instead of parton showers (MEPS),

**Table 6.** Differential hadron level dijet cross sections in the restricted kinematical range  $x_{\mathbb{P}} < 0.01$ 

Dijet cross section as a function of $Q^2$ for $x_{\mathbb{P}} < 0.01$ .							
Bin	$Q^2$ [GeV <sup>2</sup> ]		$\sigma$ [pb/GeV <sup>2</sup> ]	stat. err. [%]	syst. err. [%]	tot. err. [%]	
1	4.0	–	10.0	1.58	9.7	18.5	20.9
2	10.0	–	20.0	0.40	13.9	18.4	23.1
3	20.0	–	40.0	0.12	17.7	29.2	34.1
4	40.0	–	80.0	0.01	44.7	58.3	73.5
Dijet cross section as a function of $p_{T,jets}^*$ for $x_{\mathbb{P}} < 0.01$ .							
Bin	$p_{T,jets}^*$ [GeV]		$\sigma$ [pb/GeV]	stat. err. [%]	syst. err. [%]	tot. err. [%]	
1	4.0	–	5.0	8.3	12.0	23.9	26.8
2	5.0	–	6.0	4.7	11.0	21.3	24.0
3	6.0	–	7.5	2.0	16.0	19.1	24.9
4	7.5	–	9.0	0.3	50.0	43.2	66.1
Dijet cross section as a function of $z_{\mathbb{P}}^{(jets)}$ for $x_{\mathbb{P}} < 0.01$ .							
Bin	$z_{\mathbb{P}}^{(jets)}$		$\sigma$ [pb]	stat. err. [%]	syst. err. [%]	tot. err. [%]	
1	0.00	–	0.30	5.2	30.2	85.2	90.4
2	0.30	–	0.45	25.8	16.2	31.5	35.4
3	0.45	–	0.60	28.0	13.9	21.3	25.5
4	0.60	–	0.80	24.8	12.8	18.9	22.9
5	0.80	–	1.00	11.9	17.4	22.0	28.0
Dijet cross section as a function of $p_{T,rem}^{(\mathbb{P})}$ for $x_{\mathbb{P}} < 0.01$ .							
Bin	$p_{T,rem}^{(\mathbb{P})}$ [GeV]		$\sigma$ [pb/GeV]	stat. err. [%]	syst. err. [%]	tot. err. [%]	
1	0.0	–	0.5	24.5	10.3	26.8	28.8
2	0.5	–	1.0	11.2	12.7	24.8	27.9
3	1.0	–	3.0	1.3	16.0	58.1	60.3

**Table 7.** Differential hadron level 3-Jet cross sections

3-jet cross section as a function of $M_{123}$ .							
Bin	$M_{123}$ [GeV]		$\sigma$ [pb/GeV]	stat. err. [%]	syst. err. [%]	tot. err. [%]	
1	12.0	–	20.0	0.48	14.4	33.0	36.1
2	20.0	–	30.0	0.43	11.6	23.0	25.7
3	30.0	–	40.0	0.06	35.3	40.5	53.7
3-jet cross section as a function of $z_{\mathbb{P}}^{(3 jets)}$ .							
Bin	$z_{\mathbb{P}}^{(3 jets)}$		$\sigma$ [pb]	stat. err. [%]	syst. err. [%]	tot. err. [%]	
1	0.2	–	0.4	13.1	16.2	43.8	46.7
2	0.4	–	0.6	13.9	13.9	20.5	24.7
3	0.6	–	0.8	10.5	18.6	22.6	29.2

the predicted dijet cross sections increase in normalisation by approximately 15% (Fig. 5). The shapes of the predicted distributions, including that of  $z_{\mathbb{P}}^{(jets)}$ , are not significantly affected.

The cross section differential in  $z_{\mathbb{P}}^{(jets)}$  (Fig. 7) is also compared with predictions from different sets of pomeron parton distributions. Figure 7a shows the predictions based on the partons extracted in ‘fit 2’ and ‘fit 3’ of [3]. The parton distributions are evaluated at a scale<sup>12</sup>  $\mu^2 = Q^2 + p_T^2$ . The contribution of quark induced processes

in the predictions is small. The fraction of the cross section ascribed to resolved virtual photons, which is shown separately for ‘fit 2’ in Fig. 7a, is also small and is concentrated at low  $z_{\mathbb{P}}^{(jets)}$ . The same is true for the reggeon contribution (not shown). The predictions based on the ‘flat gluon’ or ‘fit 2’ parton densities are in very good agreement with the data. The ‘peaked gluon’ or ‘fit 3’ parameterisation leads to an overestimate of the dijet cross section at high values of  $z_{\mathbb{P}}^{(jets)}$ . The gluon distributions from which the predictions are derived are shown above the data at  $\mu^2 = 42$  GeV<sup>2</sup>, representing the mean value of  $Q^2 + p_{T,jets}^{*2}$  for the selected events. The difference in shape between the gluon distributions and the hadron level pre-

<sup>12</sup> Alternative reasonable choices of scale such as  $Q^2 + 4p_T^2$  make only small differences to the Monte Carlo predictions

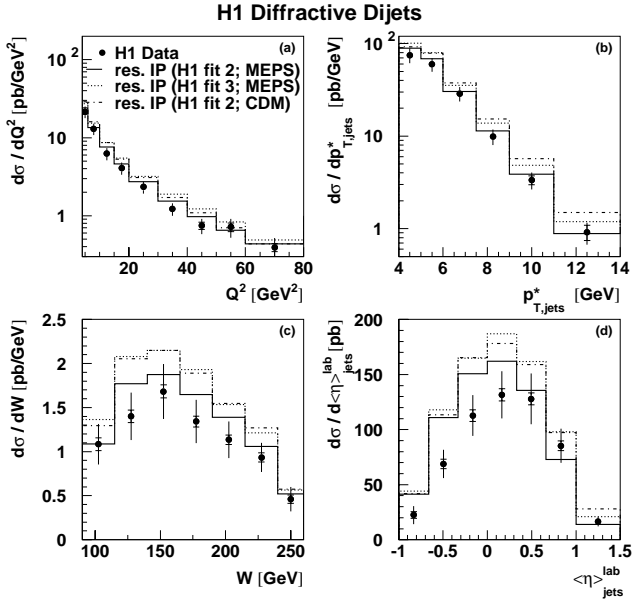


**Fig. 5a–d.** Diffractive dijet cross sections as a function of **a** the photon virtuality  $Q^2$ , **b** the mean transverse jet momentum  $p_{T,jets}^*$  in the  $\gamma^*p$  centre-of-mass frame, **c** the  $\gamma^*p$  invariant mass  $W$  and **d** the mean jet pseudorapidity in the laboratory frame  $\langle \eta \rangle_{jets}^{lab}$ . Also shown are the predictions from a resolved (partonic) pomeron model with gluon dominated pomeron parton distributions as obtained from the QCD analysis of  $F_2^{D(3)}$  by H1 [3]. The results, using both the ‘fit 2’ (‘flat gluon’) and ‘fit 3’ (‘peaked gluon’) parton distributions for the pomeron, are shown evolved to a scale  $\mu^2 = Q^2 + p_T^2$ . Resolved virtual photon contributions are added according to the SaS-2D parameterisation [48]. The prediction based on ‘fit 2’ is also shown where the colour dipole approach (CDM) for higher order QCD effects is used in place of parton showers (MEPS)

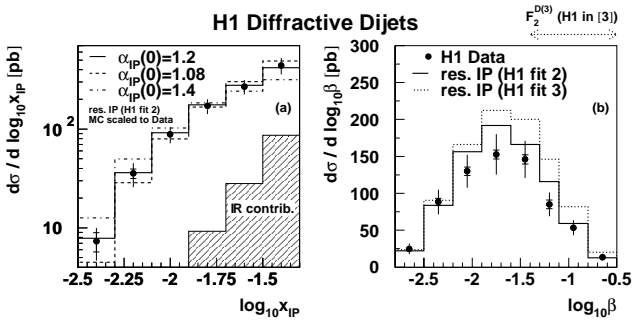


**Fig. 6a,b.** Differential diffractive dijet cross sections as functions of **a**  $\log x_p$  and **b**  $\log \beta$ . The solid curves represent the predictions of the resolved pomeron model (‘fit 2’) as described in the text with direct and resolved photon contributions. For the  $\log x_p$  distribution, the contribution from sub-leading reggeon exchange is indicated by the hatched area. The dashed and dashed-dotted histograms correspond to the cross section predictions where the value of the pomeron intercept  $\alpha_{\mathbb{P}}(0)$  in the model was changed from the default value of 1.20 to 1.08 and 1.40 respectively. For this figure, all model predictions have been scaled to the integrated cross section in the data. For the  $\log \beta$  distribution, the prediction using the ‘fit 3’ parton distributions is also shown and the range covered by the inclusive H1 measurement of  $F_2^{D(3)}$  is indicated

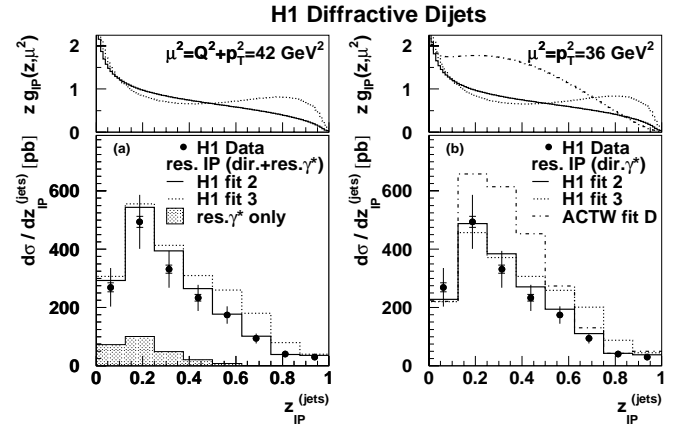


**Fig. 7a,b.** The diffractive dijet cross section as a function of  $z_{IP}^{(jets)}$ . The same data are compared to predictions of resolved pomeron models, where either **a**  $\mu^2 = Q^2 + p_T^2$  or **b**  $\mu^2 = p_T^2$  are used as renormalisation and factorisation scales. In **a**, the ‘fit 2’ (or ‘flat gluon’) and ‘fit 3’ (or ‘peaked gluon’) parameterisations based on the H1 leading order QCD fits to  $F_2^{D(3)}$  [3] are shown. Direct and resolved  $\gamma^*$  contributions are both included. The size of the resolved  $\gamma^*$  contribution in ‘fit 2’ is indicated by the shaded histogram. In **b**, where only the direct  $\gamma^*$  contributions are shown, the preferred solution ‘ACTW fit D’ of the fits from [58] is shown in addition to the H1 fits. The corresponding gluon distributions, evolved to the mean value of the respective scale used and normalised such that the pomeron flux  $f_{\mathbb{P}/p}(x_{\mathbb{P}} = 0.003, t = 0)$  is unity, are shown above the predictions

dictions reflects the kinematic range of the measurement (Table 1). The dijet data are highly sensitive to the shape of the gluon distribution, which is poorly constrained by the  $F_2^{D(3)}$  measurements. This is especially the case in the region of large momentum fractions ( $z_{\mathbb{P}}$  or  $\beta$ ), since data with  $\beta > 0.65$  were excluded from the DGLAP analysis of  $F_2^{D(3)}$ .

In Fig. 7b, the same data are compared with the models where  $p_T^2$  was chosen as the renormalisation and factorisation scale and only direct photon contributions are included. The level of agreement between the data and the simulations based on the H1 fits is similar to that in Fig. 7a. Also shown is a prediction based on the best combined fit in [58] to H1 and ZEUS  $F_2^{D(3)}$  data and ZEUS diffractive dijet photoproduction data<sup>13</sup>. Due to the different shape and normalisation of the gluon distribution in this parameterisation, the agreement with the dijet data is significantly poorer than is the case for the two H1 fits.

In general, the close agreement between the ‘fit 2’ and ‘fit 3’ parameterisations and the data can be interpreted as support for factorisable pomeron parton distributions in DIS, strongly dominated by gluons with a momentum distribution relatively flat in  $z_{\mathbb{P}}$ .

<sup>13</sup> In this parameterisation, the pomeron intercept is set to  $\alpha_{\mathbb{P}}(0) = 1.19$

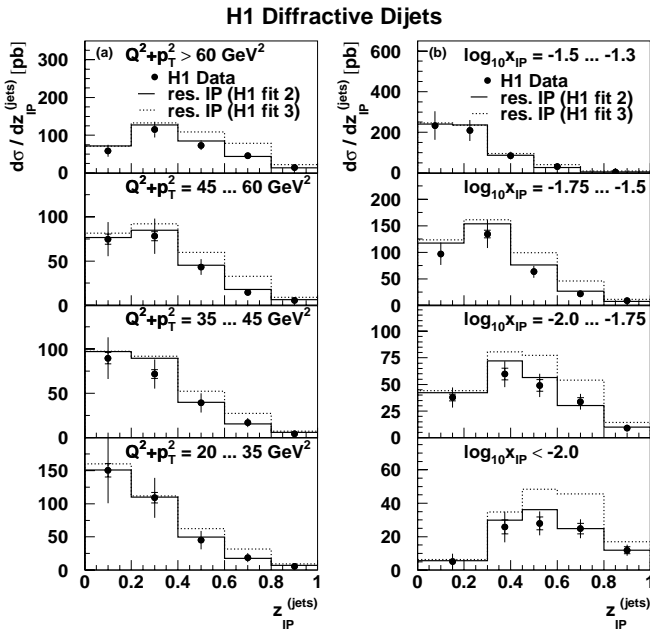


**Fig. 8a,b.** Diffractive dijet cross sections as a function of  $z_{\mathbb{P}}^{(jets)}$ , shown in four intervals of **a** the scale  $\mu^2 = Q^2 + p_T^2$  and **b**  $\log x_{\mathbb{P}}$ . The data are compared to the resolved pomeron model based on the two fits to  $F_2^{D(3)}$  from H1, including both direct and resolved  $\gamma^*$  contributions

### 5.2.2 Scale dependence, Regge factorisation and pomeron intercept

In the following, some basic assumptions of the resolved pomeron model are tested, namely the evolution of the parton distributions with scale, Regge factorisation and the universality of the pomeron intercept.

Figure 8a shows the cross section differential in  $z_{\mathbb{P}}^{(jets)}$  in four intervals of the scale  $\mu^2 = Q^2 + p_T^2$ . Even in this double differential view, the ‘fit 2’ resolved pomeron model with parton densities evolving according to the DGLAP equations gives a very good description of the data. The ‘peaked gluon’ solution overestimates the cross section at high  $z_{\mathbb{P}}^{(jets)}$  in all regions of  $\mu^2$ .

In Fig. 8b, the data are used to test Regge factorisation (7). The cross section differential in  $z_{\mathbb{P}}^{(jets)}$  is measured in four intervals of  $x_{\mathbb{P}}$ . A substantial dependence of the shape of the  $z_{\mathbb{P}}^{(jets)}$  distribution on  $x_{\mathbb{P}}$  is observed. This is dominantly a kinematic effect, since  $x_{\mathbb{P}}$  and  $z_{\mathbb{P}}^{(jets)}$  are connected via the relation  $x_{\mathbb{P}} \cdot z_{\mathbb{P}}^{(jets)} = x_p^{(jets)}$ , where  $x_p^{(jets)}$  is the proton momentum fraction which enters the hard process. The range in  $x_p^{(jets)}$  is approximately fixed by the kinematic range of the measurement. Again, the factorising resolved pomeron model describes the distributions well. Thus, at the present level of precision, the data are compatible with Regge factorisation. There is little freedom to change the pomeron intercept  $\alpha_{\mathbb{P}}(0)$  and compensate this by adjusting the gluon distribution. Fast variations of  $\alpha_{\mathbb{P}}(0)$  with  $z_{\mathbb{P}}$  are also incompatible with the data.

The value of  $\alpha_{\mathbb{P}}(0)$  controls the energy or  $x_{\mathbb{P}}$  dependence of the cross section. In the predictions of the resolved pomeron model shown in Figs. 5–8, a value of  $\alpha_{\mathbb{P}}(0) = 1.2$  is used, as obtained in the H1 analysis of  $F_2^{D(3)}$  [3]. Since this value of  $\alpha_{\mathbb{P}}(0)$  is larger than that describing soft interactions, it is interesting to investigate whether further variation takes place with the additional hard scale introduced in the dijet sample. In Fig. 6a, the effect on the shape of the predicted cross section differential in  $x_{\mathbb{P}}$  is investigated when  $\alpha_{\mathbb{P}}(0)$  is varied. As examples, the predictions with  $\alpha_{\mathbb{P}}(0) = 1.08$  (‘soft pomeron’) and  $\alpha_{\mathbb{P}}(0) = 1.4$  (approximate leading order ‘BFKL pomeron’ [35]) are shown. All predictions have been scaled to the total cross section in the data. The  $x_{\mathbb{P}}$  dependence of the data requires a value for  $\alpha_{\mathbb{P}}(0)$  close to 1.2. The values of 1.08 and 1.4 result in  $x_{\mathbb{P}}$  dependences which are steeper or flatter than the data respectively. Making a fit for  $\alpha_{\mathbb{P}}(0)$  to the shape of the  $x_{\mathbb{P}}$  cross section, assuming a flux of the form given in (9), yields a value of

$$\alpha_{\mathbb{P}}(0) = 1.17 \pm 0.03 \text{ (stat.)} \pm 0.06 \text{ (syst.)} \pm_{-0.07}^{+0.03} \text{ (model)}.$$

The model dependence uncertainty is evaluated by varying the resolved photon and the reggeon contributions in the model by  $\pm 50\%$  each, changing the pomeron gluon distribution within the range allowed by the measured  $z_{\mathbb{P}}^{(jets)}$  distribution, varying the assumed  $\alpha'_{\mathbb{P}}$  within  $0.26 \pm 0.26 \text{ GeV}^{-2}$  and varying  $b_{\mathbb{P}}$  between  $2 \text{ GeV}^{-2}$  and  $8 \text{ GeV}^{-2}$ . The effects of NLO corrections and possible pomeron-reggeon interference have not been studied. The extracted value of  $\alpha_{\mathbb{P}}(0)$  is compatible with that obtained from inclusive diffraction in a similar  $Q^2$  region, despite the fact that the jets introduce an additional hard scale.

### 5.3 Energy flow in the photon hemisphere and resolved virtual photons

As can be seen from Figs. 5–8, the data are well described by the resolved pomeron model, where a contribution from resolved virtual photons is included as described in Sect. 3.5. In this section, two observables are studied which are particularly suited to the interpretation of the data in terms of direct and resolved photon contributions.

As in the case of real photoproduction analyses (see e.g. [59]), a quantity  $x_{\gamma}$  is defined as the fraction of the photon momentum which enters the hard scattering. If the 4-vector of the parton from the photon entering the hard scattering is labelled  $u$ , then

$$x_{\gamma} = \frac{P \cdot u}{P \cdot q}. \quad (16)$$

Direct photon events satisfy  $x_{\gamma} \equiv 1$  by definition. Events where the photon is resolved have  $x_{\gamma} < 1$ . At the hadron level, an observable  $x_{\gamma}^{(jets)}$  can be constructed by measuring the ratio of the summed  $E - p_z$  of the two jets to the total  $E - p_z$ :

$$x_{\gamma}^{(jets)} = \frac{\sum_{jets} E - p_z}{\sum_{all} E - p_z}. \quad (17)$$

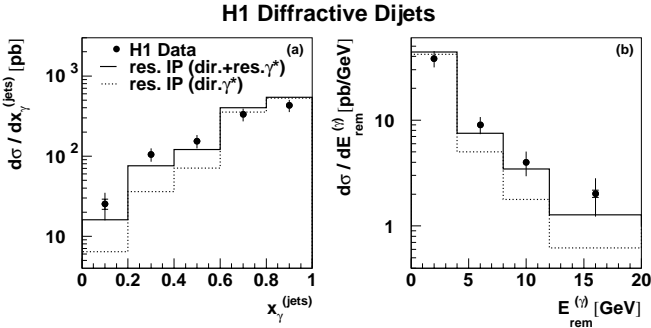


**Fig. 9a,b.** Differential diffractive dijet cross sections as a function of **a**  $x_\gamma^{(jets)}$ , an estimator for the photon momentum fraction entering the hard scattering process, and **b**  $E_{rem}^{(\gamma)}$ , the summed hadronic final state energy not belonging to the two highest  $p_T^*$  jets in the photon hemisphere of the  $\gamma^*P$  centre-of-mass frame. The data are compared to the resolved pomeron model (‘fit 2’) with and without an additional contribution from resolved virtual photons, parameterised according to the SaS-2D photon parton distributions

The observable  $x_\gamma^{(jets)}$  correlates well with the parton level  $x_\gamma$  and is reconstructed with a resolution of approximately 12% relative to the hadron level definition. The cross section differential in  $x_\gamma^{(jets)}$  is shown in Fig. 9a. The distribution is peaked at values around 1 but there is also a sizeable cross section at lower  $x_\gamma^{(jets)}$  values. The prediction of the resolved pomeron model with only direct photon contributions describes the high  $x_\gamma^{(jets)}$  region, but lies significantly below the data at low values of  $x_\gamma^{(jets)}$ . The prediction is non-zero in this region only because of migrations from the parton level value of  $x_\gamma$  to the hadron level quantity  $x_\gamma^{(jets)}$ . If the contribution from resolved photons is included, a much improved description of the data is achieved. The total predicted dijet cross section then increases by 17%.

The part of the hadronic final state not associated to the two highest  $p_T^*$  jets is best studied in the  $\gamma^*P$  centre-of-mass frame (see Sect. 5.1). Hadronic final state particle production outside the two highest  $p_T^*$  jets can originate from jet resolution effects, possible photon and pomeron remnants or from higher order QCD diagrams. In order to further investigate the energy in the photon hemisphere, a new observable  $E_{rem}^{(\gamma)}$  is constructed.  $E_{rem}^{(\gamma)}$  is defined as the energy sum of all final state hadrons in the photon hemisphere ( $\eta^\dagger < 0$ ) which lie outside the two highest  $p_T^*$  jet cones. The cross section is shown differentially in  $E_{rem}^{(\gamma)}$  in Fig. 9b. The distribution falls quickly as  $E_{rem}^{(\gamma)}$  increases, indicating the dominance of direct photon scattering. The description at high  $E_{rem}^{(\gamma)}$  values (corresponding to  $x_\gamma < 1$ ) is again much improved by adding the resolved  $\gamma^*$  contribution.

The presence of resolved virtual photon contributions is also suggested by the energy flow backward of the jets (corresponding to the photon direction) in the jet profiles (Fig. 3). Similarly, the transverse energy not associated with the jets in the  $\eta^\dagger < 0$  hemisphere of the  $\gamma^*P$  sys-

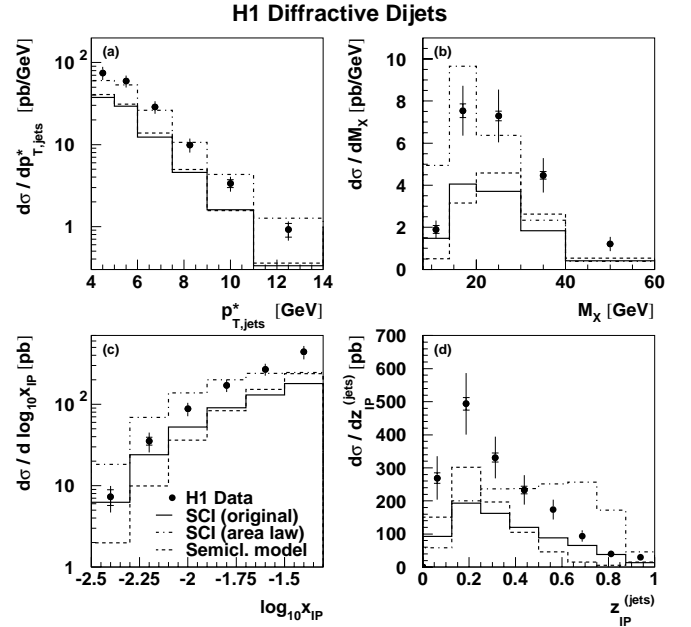


**Fig. 10a–d.** Differential dijet cross sections as functions of **a**  $p_{T,jets}^*$ , **b**  $M_X$ , **c**  $\log x_{IP}$  and **d**  $z_{IP}^{(jets)}$ . The data are compared to the original version of the Soft Colour Interaction (SCI) model, labelled ‘SCI (original)’, the prediction of the refined SCI version based on a generalised area law for string reconnections, labelled ‘SCI (area law)’, and to the semiclassical model

(Fig. 4a), is best described when the resolved photon contribution is added. Good descriptions of these distributions cannot be achieved by adjusting the diffractive gluon distribution. The resolved virtual photon contributions can be viewed as an approximation to NLO QCD diagrams and/or contributions without strong  $k_T$  ordering. The possible presence of such effects will be investigated further in Sect. 5.5.

#### 5.4 Soft colour neutralisation models

The Soft Colour Interactions (SCI) and semiclassical models (Sect. 3.4) both give a reasonably good description of inclusive diffraction at HERA with a small number of free parameters. In Fig. 10, the predictions of these models are compared with the dijet cross sections as functions of  $p_{T,jets}^*$ ,  $M_X$ ,  $\log x_{IP}$  and  $z_{IP}^{(jets)}$ . With the exception of the cross section differential in  $M_X$ , the data shown are identical to those in earlier figures. The original version of SCI gives a reasonable description of the shapes of the differential distributions of the dijet data, but the overall cross section is too low by a factor of about 2. The refined version of the SCI model, based on a generalised area law for string rearrangements, gives an improved description of  $F_2^{D(3)}$  at low  $Q^2$ . It also reproduces the normalisation of the dijet cross sections much better than the original version. However, the shapes of the differential distributions are not described, with the exception of  $p_{T,jets}^*$ .

The semiclassical model gives a good description of the shapes of the distributions, but the total predicted dijet cross section is only around half that measured. The free parameters of the semiclassical model were determined using only  $F_2^{D(3)}$  data in the region  $x_{\mathbb{P}} < 0.01$ . Even at low  $x_{\mathbb{P}}$ , the predictions lie significantly below the dijet data (Fig. 10c). It is possible that the inclusion of NLO terms would improve the description of the data by the semiclassical model.

### 5.5 Colour dipole and 2-gluon exchange models

In this section, the saturation and BJLW models (Sect. 3.3), based on the ideas of dipole cross sections and 2-gluon exchange, are compared with the dijet data. Because of the nature of the 2-gluon models, only final state parton showers are included in the simulations. A restricted data sample with the additional cut

$$x_{\mathbb{P}} < 0.01 \quad (18)$$

is studied, because the calculations were carried out under the assumption of low  $x_{\mathbb{P}}$  to avoid contributions from secondary reggeon exchanges and ensure that the proton parton distributions are gluon dominated. Applying this additional restriction reduces the number of events in the data sample by a factor of approximately 4.

The resolved pomeron model implies the presence of a soft pomeron remnant. The same is true for  $q\bar{q}g$  production within the saturation model where the gluon behaves in a ‘remnant-like’ manner, due to the  $k_T$ -ordering condition imposed in the calculations. By contrast, the  $q\bar{q}g$  calculation within the BJLW model imposes high transverse momenta on all three partons and is not restricted to  $k_T$ -ordered configurations. Any ‘remnant’ system beyond the dijets in this model is thus expected to have relatively large  $p_T$ . To gain more insight into the properties of the part of the hadronic final state not belonging to the jets, a new observable  $p_{T,rem}^{(\mathbb{P})}$  is introduced. By analogy with the definition of  $E_{rem}^{(\gamma)}$  (Sect. 5.3), this variable measures the transverse momentum of all hadronic final state particles in the pomeron hemisphere of the  $\gamma^*\mathbb{P}$  centre-of-mass frame ( $\eta^\dagger > 0$ ) not belonging to the two highest  $p_T^*$  jets.

Dijet cross sections for the region  $x_{\mathbb{P}} < 0.01$  differential in  $Q^2$ ,  $p_{T,jets}^*$ ,  $z_{\mathbb{P}}^{(jets)}$  and  $p_{T,rem}^{(\mathbb{P})}$  are shown in Fig. 11. They are compared with the predictions of the saturation, BJLW and resolved pomeron (‘fit 2’) models. The saturation model is able to reproduce the shapes of the measured cross sections, though the overall predicted dijet rate is too low by a factor of approximately 2. The normalisation of the saturation model is fixed from the fit to inclusive  $F_2$  data and by the assumed  $e^{6t}$  dependence for diffractive processes. The total predicted dijet cross section would increase whilst preserving a good description of  $F_2^{D(3)}$  if the  $t$  dependence were found to be harder for dijet production than for inclusive diffraction.

In the BJLW model, the contribution from  $q\bar{q}$  states alone is negligibly small even at large values of  $z_{\mathbb{P}}$ . This

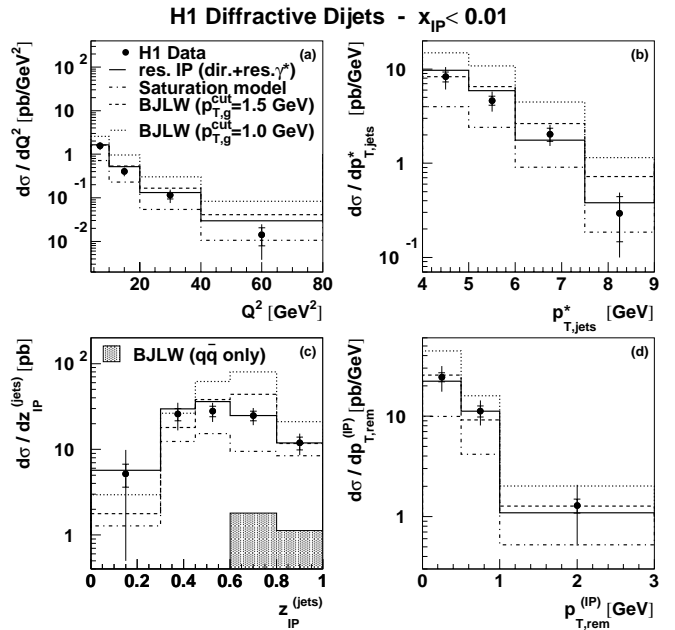


**Fig. 11a–d.** Diffractive dijet cross sections in the restricted kinematic range  $x_{\mathbb{P}} < 0.01$ , shown as functions of **a**  $Q^2$ , **b**  $p_{T,jets}^*$ , **c**  $z_{\mathbb{P}}^{(jets)}$  and **d**  $p_{T,rem}^{(\mathbb{P})}$ , the latter denoting the summed transverse momentum of the final state particles not belonging to the two highest  $p_T^*$  jets and located in the pomeron hemisphere of the  $\gamma^*\mathbb{P}$  centre-of-mass frame. The data are compared to the saturation, BJLW and resolved pomeron (‘fit 2’, direct and resolved virtual photons) models. For the BJLW model, the contribution from  $q\bar{q}$  states alone and the sum of the  $q\bar{q}$  and  $q\bar{q}g$  contributions for two different values of the  $p_T$  cut-off for the gluon  $p_{T,g}^{cut}$  are shown

is in accordance with the expectation for high  $p_T$ , high  $M_X$  diffractive final states. The predicted  $q\bar{q}g$  contribution is much larger. The normalisation of the BJLW model for  $q\bar{q}g$  production can be controlled by tuning the lower cut-off on the transverse momentum of the gluon  $p_{T,g}^{cut}$  in the calculations. If this cut-off is set to 1.5 GeV, the total cross section for dijet production with  $x_{\mathbb{P}} < 0.01$  is approximately correct in the model. Lowering  $p_{T,g}^{cut}$  to 1.0 GeV leads to a prediction significantly above the measured cross section. The description of the shapes of the differential cross sections is reasonable apart from small discrepancies in the  $z_{\mathbb{P}}^{(jets)}$  distribution. The differences between the predictions of the saturation and BJLW models may originate from the different parameterisations of  $\mathcal{F}(x, k_T^2)$ , the different treatments of non- $k_T$ -ordered configurations or from the assumed  $t$  dependences.

The resolved pomeron model, in which the non- $k_T$ -ordered resolved photon contributions are small in the low  $x_{\mathbb{P}}$  region, continues to give the best description of all observables, including the  $p_{T,rem}^{(\mathbb{P})}$  distribution. The good description of the  $p_{T,rem}^{(\mathbb{P})}$  distribution by both the resolved pomeron and the BJLW models indicates that the present data are not easily able to discriminate between models with a soft ‘remnant’ and those with a third high- $p_T$  parton.

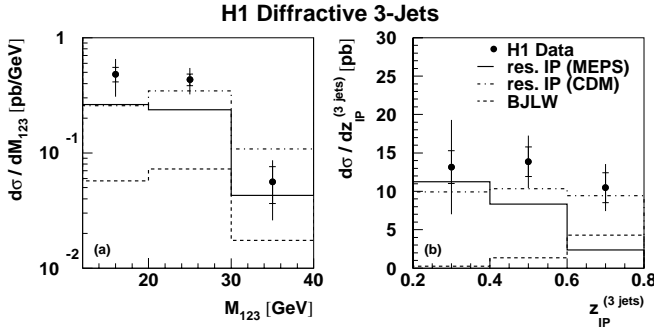


**Fig. 12a,b.** Differential cross sections for diffractive 3-jet production as functions of **a** the 3-jet invariant mass  $M_{123}$  and **b** the corresponding  $z_{\mathbb{P}}$ -variable  $z_{\mathbb{P}}^{(3 jets)}$ , measuring the colourless exchange momentum fraction which enters the hard interaction. The data are compared with the resolved pomeron model with two different approaches for higher order QCD diagrams, the parton shower model (labelled ‘MEPS’) and the colour dipole approach (labelled ‘CDM’). The ‘H1 fit 2’ parameterisation is used and direct and resolved virtual photon contributions are included. The BJLW model is also shown, including  $q\bar{q}$  and  $q\bar{q}g$  contributions, with the cut-off for the gluon  $p_{T,g}^{cut}$  set to 1.5 GeV

### 5.6 3-Jet production

The diffractive production of three high- $p_T$  jets as components of the  $X$  system has been investigated. Except for the requirement on the number of jets, the analysis is identical to the dijet analysis, such that no requirements are made on possible hadronic activity beyond the jets. In Fig. 12, the measured 3-jet cross sections are presented as functions of the 3-jet invariant mass  $M_{123}$  and

$$z_{\mathbb{P}}^{(3 jets)} = \frac{Q^2 + M_{123}^2}{Q^2 + M_X^2}, \quad (19)$$

which, similarly to  $z_{\mathbb{P}}^{(jets)}$  for dijet events, is a measure of the fraction of the energy of the  $X$  system which is contained in the jets. The  $z_{\mathbb{P}}^{(3 jets)}$  cross section is measured up to 0.8. With the present statistics, it is not possible to extract a cross section for the interesting region  $0.8 < z_{\mathbb{P}}^{(3 jets)} \leq 1.0$ , which corresponds approximately to ‘exclusive’ 3-jet production. The measured  $z_{\mathbb{P}}^{(3 jets)}$  cross section demonstrates that additional hadronic activity beyond the jets is typically present even in the 3-jet sample.

The data are compared with the resolved pomeron model (‘fit 2’), with the hard interaction evaluated at a scale  $\mu^2 = Q^2 + p_T^2$ . Direct and resolved  $\gamma^*$  contributions are included. Because the leading order for 3-parton final states is  $\mathcal{O}(\alpha_s^2)$ , two different approximations for higher order QCD diagrams are considered here, the parton shower model (MEPS) and the colour dipole approach (CDM). The measured cross sections are well described when using CDM. The MEPS simulation tends to lie below the data at low  $M_{123}$  or high  $z_{\mathbb{P}}^{(3 jets)}$ .

The BJLW calculation with  $p_{T,g}^{cut} = 1.5$  GeV is not able to accommodate the observed rate of 3-jet events. The

predicted cross section increases towards the high  $z_{\mathbb{P}}^{(3 jets)}$  regime of exclusive 3-jet production. For kinematic reasons, the 3-jet sample originates from the region  $x_{\mathbb{P}} > 0.01$ , where contributions from the proton quark distributions and secondary exchanges, which are not included in the 2-gluon models, can no longer be neglected. An improvement in the predictions of dipole models may also come through the inclusion of higher multiplicity photon fluctuations such as  $q\bar{q}gg$ , which have not yet been calculated.

## 6 Summary and final remarks

An analysis of the production of jets as components of the dissociating photon system  $X$  in the diffractive DIS reaction  $ep \rightarrow eXY$  has been presented for  $4 < Q^2 < 80$  GeV<sup>2</sup>,  $x_{\mathbb{P}} < 0.05$ ,  $p_{T,jet}^* > 4$  GeV,  $M_Y < 1.6$  GeV and  $|t| < 1.0$  GeV<sup>2</sup>. The kinematic range has been extended to lower  $Q^2$  and  $p_{T,jet}^*$  compared to previous measurements [8] and the statistical precision is much improved. Cross sections for the production of three high transverse momentum jets have been measured for the first time in diffraction.

The observed dijet events typically exhibit a structure where, in addition to the reconstructed jets, the  $X$  system contains hadronic energy with transverse momentum below the jet scale. The dijet invariant mass is thus generally smaller than  $M_X$ . Viewed in the proton rest frame, the data clearly require the dominance of higher multiplicity photon fluctuations (e.g.  $q\bar{q}g$ ) over the simplest  $q\bar{q}$  configuration. Considered in the proton infinite momentum frame, the data show that the diffractive gluon distribution is much larger than the quark distribution.

The data can be described by a ‘resolved partonic pomeron’ model, with diffractive parton distributions extracted from  $F_2^{D(3)}$  data. The good description from this model strongly supports the validity of diffractive hard scattering factorisation in DIS. The dominant contribution in the model arises from a diffractive exchange with factorising  $x_{\mathbb{P}}$  dependence (‘Regge’ factorisation). A value of  $\alpha_{\mathbb{P}}(0) = 1.17 \pm 0.03$  (stat.)  $\pm 0.06$  (syst.)  $^{+0.03}_{-0.07}$  (model) is obtained for the intercept of the leading trajectory from fits to the dijet data. The compatibility of the data with QCD hard scattering and Regge factorisation contrasts with the observed strong factorisation breaking when diffractive  $ep$  and  $p\bar{p}$  data are compared [15, 58]. The dijet data give the best constraints to date on the pomeron gluon distribution. The data require a large fraction (80–90%, as obtained in [3]) of the pomeron momentum to be carried by gluons with a momentum distribution which is comparatively flat in  $z_{\mathbb{P}}$ . Predictions derived from the ‘flat gluon’ (or ‘fit 2’) parameterisation in [3], with higher order QCD effects modelled using parton showers, are in remarkably good agreement with all aspects of the dijet data with the single exception of the  $\langle \eta \rangle_{jets}^{lab}$  dependence. The level of agreement between the resolved pomeron model and the data is better than that obtained from leading order predictions for inclusive  $ep$  dijet data (e.g. [60]), where

the NLO corrections are approximately 40% in a similar region of  $Q^2$  and  $p_{T,jets}^*$ .

The two versions of the Soft Colour Interactions (SCI) model are not able to reproduce the overall dijet rate and the shapes of the differential cross sections at the same time. The similarly motivated semiclassical model in its present (leading order) form achieves a good description of the shapes of the differential distributions but underestimates the total dijet cross section.

Models based on colour dipole cross sections and 2-gluon exchange have been compared with the dijet data in the restricted region  $x_{\mathbb{P}} < 0.01$ . The saturation model, which takes only  $k_T$  ordered configurations into account, describes the shapes of the jet distributions but underestimates the overall cross section. The normalisation of the BJLW model, in which strong  $k_T$  ordering is not imposed, is close to the data if a cut-off for the gluon transverse momentum of  $p_{T,g}^{cut} = 1.5$  GeV is chosen for the  $q\bar{q}g$  contribution. The shapes of the differential distributions are reasonably well described.

Strong conclusions cannot yet be drawn from the 3-jet production cross sections, because of the limited statistical accuracy and the kinematic restriction to large  $x_{\mathbb{P}}$  implied by the requirement of three high  $p_T$  jets. At the present level of precision, the partonic pomeron predictions based on the ‘fit 2’ parameterisation in [3] are in good agreement with the 3-jet cross sections, provided the CDM model of higher order QCD effects is used. The BJLW model is unable to reproduce the rate of observed 3-jet events when  $p_{T,g}^{cut}$  is kept fixed at 1.5 GeV.

In conclusion, diffractive jet production has been shown to be a powerful tool to gain insight into the underlying QCD dynamics of diffraction, in particular the role of gluons. The jet cross sections are sensitive to differences between phenomenological models which all give a reasonable description of  $F_2^{D(3)}$ . Models based on fully factorisable diffractive parton distributions continue to be successful. Progress in calculations based on 2-gluon exchange has led to improved agreement with the data.

*Acknowledgements.* We are grateful to the HERA machine group whose outstanding efforts have made and continue to make this experiment possible. We thank the engineers and technicians for their work in constructing and now maintaining the H1 detector, our funding agencies for financial support, the DESY technical staff for continual assistance, and the DESY directorate for the hospitality which they extend to the non DESY members of the collaboration. We have benefited from interesting discussions with J. Bartels, A. Hebecker and M. McDermott.

## References

1. ZEUS Collaboration, M. Derrick et al., Phys. Lett. **B 315** (1993) 481. H1 Collaboration, T. Ahmed et al., Nucl. Phys. **B 429** (1994) 477
2. H1 Collaboration, T. Ahmed et al., Phys. Lett. **B 348** (1995) 681
3. H1 Collaboration, C. Adloff et al., Z. Phys. **C 76** (1997) 613
4. ZEUS Collaboration, J. Breitweg et al., Eur. Phys. J. **C 1** (1998) 81; ZEUS Collaboration, J. Breitweg et al., Eur. Phys. J. **C 6** (1999) 43
5. H1 Collaboration, C. Adloff et al., Eur. Phys. J. **C 1** (1998) 495; H1 Collaboration, C. Adloff et al., Phys. Lett. **B 428** (1998) 206; H1 Collaboration, C. Adloff et al., Eur. Phys. J. **C 5** (1998) 439
6. ZEUS Collaboration, J. Breitweg et al., Phys. Lett. **B 421** (1998) 368
7. ZEUS Collaboration, J. Breitweg et al., Eur. Phys. J. **C 5** (1998) 41
8. H1 Collaboration, C. Adloff et al., Eur. Phys. J. **C 6** (1999) 421
9. M. Ryskin, Sov. J. Nucl. Phys. **52** (1990) 529; N. Nikolaev, B. Zakharov, Z. Phys. **C 53** (1992) 331
10. A. Mueller, Nucl. Phys. **B 335** (1990) 115; M. Diehl, Z. Phys. **C 66** (1995) 181
11. J. Bartels, H. Lotter, M. Wüsthoff, Phys. Lett. **B 379** (1996) 239 and erratum-ibid. **B 382** (1996) 449; J. Bartels, C. Ewerz, H. Lotter, M. Wüsthoff, Phys. Lett. **B 386** (1996) 389; H. Lotter, Phys. Lett. **B 406** (1997) 171
12. J. Bartels, H. Jung, M. Wüsthoff, Eur. Phys. J. **C 11** (1999) 111; J. Bartels, H. Jung, A. Kyrleis: Massive  $c\bar{c}g$ -Production in Diffractive DIS, hep-ph/0010300
13. UA8 Collaboration, R. Bonino et al., Phys. Lett. **B 211** (1988) 239; UA8 Collaboration, A. Brandt et al., Phys. Lett. **B 297** (1992) 417
14. CDF Collaboration, F. Abe et al., Phys. Rev. Lett. **79** (1998) 2636; CDF Collaboration, F. Abe et al., Phys. Rev. Lett. **80** (1998) 1156
15. CDF Collaboration, T. Affolder et al., Phys. Rev. Lett. **84** (2000) 5043
16. D0 Collaboration, B. Abbott et al.: Hard Single Diffraction in  $p\bar{p}$  Collisions at 630 and 1800 GeV, hep-ex/9912061, submitted to Phys. Rev. Lett.
17. J. Collins, Phys. Rev. **D 57** (1998) 3051 and erratum-ibid. **D 61** (2000) 019902
18. G. Ingelman, P. Schlein, Phys. Lett. **B 152** (1985) 256
19. K. Golec-Biernat, M. Wüsthoff, Phys. Rev. **D 59** (1999) 014017; K. Golec-Biernat, M. Wüsthoff, Phys. Rev. **D 60** (1999) 114023
20. F. Low, Phys. Rev. **D 12** (1975) 163; S. Nussinov, Phys. Rev. Lett. **34** (1975) 1286
21. W. Buchmüller, T. Gehrmann, A. Hebecker, Nucl. Phys. **B 537** (1999) 477
22. A. Edin, G. Ingelman, J. Rathsman, Phys. Lett. **B 366** (1996) 371; A. Edin, G. Ingelman, J. Rathsman, Z. Phys. **C 75** (1997) 57
23. J. Rathsman, Phys. Lett. **B 452** (1999) 364
24. J. Bjorken, J. Kogut, Phys. Rev. **D 8** (1973) 1341. G. Bertsch, S. Brodsky, A. Goldhaber, J. Gunion, Phys. Rev. Lett. **47** (1981) 297
25. W. Buchmüller, A. Hebecker, M. McDermott, Phys. Lett. **B 410** (1997) 304
26. L. Trentadue, G. Veneziano, Phys. Lett. **B 323** (1994) 201
27. A. Berera, D. Soper, Phys. Rev. **D 50** (1994) 4328
28. M. Grazzini, L. Trentadue, G. Veneziano, Nucl. Phys. **B 519** (1998) 394
29. V. Gribov, L. Lipatov, Sov. J. Nucl. Phys. **15** (1972) 438, 675; Y. Dokshitzer, Sov. Phys. JETP **46** (1977) 641; G. Altarelli, G. Parisi, Nucl. Phys. **B 126** (1977) 298

30. F. Hautmann, Z. Kunszt, D. Soper, Phys. Rev. Lett. **81** (1998) 3333
31. A. Donnachie, P. Landshoff, Phys. Lett. **B 296** (1992) 227; J. Cudell, K. Kang, S. Kim, Phys. Lett. **B 395** (1997) 311
32. N. Nikolaev, B. Zakharov, Z. Phys. **C 49** (1990) 607
33. M. McDermott, The dipole picture of small- $x$  physics, hep-ph/0008260
34. J. Bartels, J. Ellis, H. Kowalski, M. Wüsthoff, Eur. Phys. J. **C 7** (1999) 443
35. E. Kuraev, L. Lipatov, V. Fadin, Sov. Phys. JETP **45** (1977) 199; Y. Balitskii, L. Lipatov, Sov. J. Nucl. Phys. **28** (1978) 822; L. Lipatov, Sov. Phys. JETP **63** (1986) 904
36. J. Forshaw, G. Kerley, G. Shaw, Phys. Rev. **D 60** (1999) 074012; L. Frankfurt, V. Guzey, M. McDermott, M. Strikman: Unitarity and the QCD-improved dipole picture, hep-ph/9912547
37. M. Glück, E. Reya, A. Vogt, Z. Phys. **C 67** (1995) 433
38. A. Donnachie, P. Landshoff, Nucl. Phys. **B 244** (1984) 322
39. A. Hebecker, Nucl. Phys. **B 505** (1997) 349
40. H. Jung, Comp. Phys. Commun. **86** (1995) 147. (see also <http://www.desy.de/~jung/rapgap.html>)
41. J. Owens, Phys. Rev. **D 30** (1984) 943
42. N. Nikolaev: Intrinsic  $k_{\perp}$  in the Pomeron in Monte Carlo Generators for HERA Physics, A. Doyle, G. Grindhammer, G. Ingelman, H. Jung (eds.), DESY-PROC-1999-02 (1999) 377
43. M. Bengtsson, T. Sjöstrand, Z. Phys. **C 37** (1988) 465
44. G. Gustafson, Phys. Lett. **B 175** (1986) 453; G. Gustafson, U. Petterson, Nucl. Phys. **B 306** (1988) 746; B. Andersson, G. Gustafson, L. Lönnblad, U. Petterson, Z. Phys. **C 43** (1989) 625; B. Andersson, G. Gustafson, L. Lönnblad, Nucl. Phys. **B 339** (1990) 393
45. L. Lönnblad, Comp. Phys. Commun. **71** (1992) 15
46. T. Sjöstrand, Comp. Phys. Commun. **82** (1994) 74
47. A. Kwiatkowski, H. Spiesberger, H. Möhring, Comp. Phys. Commun. **69** (1992) 155
48. G. Schuler, T. Sjöstrand, Z. Phys. **C 68** (1995) 607; G. Schuler, T. Sjöstrand, Phys. Lett. **B 376** (1996) 193
49. H1 Collaboration, C. Adloff et al., Eur. Phys. J. **C 13** (2000) 397
50. A. Edin, G. Ingelman, J. Rathsman, Comp. Phys. Commun. **101** (1997) 108
51. F.-P. Schilling: Diffractive Jet Production in Deep-Inelastic  $e^+p$  Collisions at HERA, Ph.D. Thesis, University of Heidelberg (Germany), in preparation. Will be available from [http://www-h1.desy.de/publications/theses\\_list.html](http://www-h1.desy.de/publications/theses_list.html)
52. H1 Collaboration, I. Abt et al., Nucl. Instrum. Methods **A 386** (1997) 310 and 348
53. H1 Collaboration, C. Adloff et al., Z. Phys. **C 74** (1997) 221
54. CDF Collaboration, F. Abe et al., Phys. Rev. **D 45** (1992) 1448
55. B. List: Diffraktive  $J/\psi$ -Produktion in Elektron-Proton-Stößen am Speicherring HERA, Diploma Thesis, Tech. Univ. Berlin (1993), unpublished; B. List, A. Mastroberardino: DIFFVM: A Monte Carlo Generator for diffractive processes in ep scattering in Monte Carlo Generators for HERA Physics, A. Doyle, G. Grindhammer, G. Ingelman, H. Jung (eds.), DESY-PROC-1999-02 (1999) 396
56. J. Bromley et al.: HzTool: A Package for Monte Carlo - Data Comparison at HERA in Future Physics at HERA, G. Ingelman, A. De Roeck, R. Klanner (eds.), Proc. of the Workshop, DESY (1996), 611. (see also <http://www.desy.de/~h01rtc/hztool.html>)
57. H1 Collaboration, C. Adloff et al., Eur. Phys. J. **C 6** (1999) 587
58. L. Alvero, J. Collins, J. Terron, J. Whitmore, Phys. Rev. **D 59** (1999) 074022; L. Alvero, J. Collins, J. Whitmore: Tests of Factorisation in Diffractive Charm Production and Double Pomeron Exchange, hep-ph/9806340
59. ZEUS Collaboration, J. Breitweg et al., Eur. Phys. J. **C 11** (1999) 35; H1 Collaboration, C. Adloff et al., Phys. Lett. **B 483** (2000) 36
60. H1 Collaboration, C. Adloff et al., Eur. Phys. J. **C 13** (2000) 415